

This is a non-peer reviewed preprint submitted to EarthArXiv. Please note that subsequent versions of this manuscript may have slightly different content.

A simplified physics model for estimating subsurface CO₂ storage resources constrained by fault slip potential

Iman R. Kivi^{1,*}, Silvia De Simone², Samuel Krevor¹

¹Department of Earth Science and Engineering, Imperial College London, London, UK

²Institute of Environmental Assessment and Water Research, Spanish National Research Council (IDAEA-CSIC), Barcelona, Spain

*Email of the corresponding author: i.rahimzadeh-kivi@imperial.ac.uk

Abstract

Carbon Capture and Storage (CCS) at rates of several gigatonnes (Gt) per year may be needed to mitigate climate change. However, one major uncertainty is that the risk of injection-induced earthquakes may grow with this scale of deployment. In this work, we develop a tool, named CO2BLOCKSEISM, which uses simplified physics models to screen subsurface storage resources constrained by fault slip potential at regional scales. The tool relies on (1) analytical solutions of the pressure response of saline aquifers to multi-site CO₂ injection at time-varying rates and (2) a Monte Carlo-type probabilistic model for evaluating the probability of fault slip incorporating uncertainties in geomechanical variables at the basin scale. Integration of the two modules yields the temporal evolution of slip probability for mapped faults. We validate the approach against seismic activity in Oklahoma caused by basin-wide, low-pressure subsurface wastewater disposal at equivalent rates to large-scale CCS. We show that CO2BLOCKSEISM can capture key features of induced seismicity in this region. We apply the methodology to the southern Utsira Formation, Norway. We find approximately 12.5 Gt CO₂ can be stored in this region over 50 years of

continuous injection while maintaining the stability of major faults that could otherwise induce felt earthquakes. The use of fault-slip potential as a limiting condition may enable a more restrictive and realistic estimate of the potential for rates of scale-up for CO₂ storage regionally and globally.

Keywords: Climate change; Fault reactivation; Gigatonne-scale CO₂ storage; Induced seismicity; Storage resource assessment

Highlights

- Induced seismicity could be a limiting factor to subsurface CO₂ storage resources.
- We develop a tool for screening fault stability controls on regional storage resources.
- The tool CO2BLOCKSEISM enables more realistic estimates of the rate of CO₂ storage scale-up.
- Estimates of storage resources need to be updated with our knowledge of the subsurface.

1. Introduction

Energy systems projected in global pathways toward mitigating climate change rely heavily on carbon capture and storage (CCS) (IPCC, 2018). Accordingly, amounts of CO₂ to be stored deep underground are projected to reach annual rates as large as several gigatonnes (Gt) by mid-century (Zahasky and Krevor, 2020; Ringrose et al., 2021). The proposed deployment rates entail a substantial scale-up of current industrial practices, which do not cumulatively exceed 40 megatonnes (Mt) per year (Zhang et al., 2022). Although CCS at the Mt scale has been extensively

demonstrated, achieving Gt-scale storage rates faces a number of fundamental challenges arising from the availability and use of subsurface storage resources (Herzog, 2011; Krevor et al., 2023).

One of the main limiting factors to CO₂ storage resources is constrained reservoir injectivity and the associated pressure build-up effects (Bachu, 2015). Excess overpressure promotes brine leakage through the caprock into protected shallow aquifers (Birkholzer et al., 2009; Kivi et al., 2022) and may give rise to fault rupture, increasing the likelihood of felt-induced earthquakes or CO₂ migration back toward the surface (Fig. 1, Rutqvist, 2012; Vilarrasa et al., 2019). Such pressure constraints may be more pronounced where pressure fronts from multiple injection sites at regional deployment interfere or reservoir-bounding rock layers do not sufficiently permeate the displaced resident brine (Ehlig-Economides and Economides, 2010; Person et al., 2010; Ringrose and Meckel, 2019; Chatelan et al., 2023). Simplified physics models provide useful tools for rapid analysis of reservoir pressurization in response to time-varying storage resource use with minimal information from the subsurface. This precludes the need to always rely on numerical reservoir simulations, which are data- and computationally-intensive (Huang et al., 2014).

Simplified physics models span a range of complexities. Static approaches, conceptually corresponding to uniform distribution of the injected CO₂ into the reservoir, estimate overpressure from the consideration of fluid and pore space compressibilities alone (Zhou et al., 2008; van der Meer and Yavuz, 2009). These models may only suit small, bounded reservoirs of high permeability, permitting fast redistribution of pore pressure across the reservoir area. Increasing in complexity, analytical models have been developed to describe CO₂ fluid dynamics, including the dynamic spatial evolution of the pressure distribution in bounded and unbounded reservoirs (Nordbotten et al., 2005; Dentz and Tartakovsky, 2009; Mathias et al., 2011; Vilarrasa et al., 2010).

Initially derived for single-site injections, these solutions have been extended to multi-site injection scenarios using the superposition principle (Huang et al., 2014; Ganjdanesh and Hosseini, 2018; De Simone et al., 2019; De Simone and Krevor, 2021; Firoozmand and Leonenko, 2022). The developed tools have enabled first-order assessment of pressure controls on storage capacities in a number of basins around the world (Rodriguez Calzado et al., 2022; Qin et al., 2023; Smith et al., 2024).

The existing methodologies of screening basin-wide storage resources are constrained by the rock – either reservoir or caprock – fracture limits to pressure buildup also referred to as injectivity constraints. These approaches commonly consider the maximum pressure build-up in the whole study area to assess the rock fracturing behavior (Szulczewski et al., 2012; Gasda et al., 2017; Elenius et al., 2018). Another conservative assumption adopted in the resource screening tool CO2BLOCK that we develop further in this work is to assume cohesionless rock (De Simone and Krevor, 2021). This is conceptually equivalent to the assumption that a plane of weakness, such as a fault, optimally oriented to slip, crosses the zone of highest pressure build-up. Although this simplistic approach partially addresses constraints imposed by fault slip on the storage capacity, there exist several motivations for explicitly accounting for the spatial variations of fault stability. First, the state of stress and the relative orientation of the faults, which impose primary controls on the propensity of the faults to slip, may exhibit large variations over regional scales (Walsh and Zoback, 2016; Snee and Zoback, 2018). Second, neither the hazard nor the risk associated with fault slip are proportionately distributed. The magnitude and frequency of the seismic events, which are principally controlled by fault distributions and attributes, serve as key parameters in the assessment of induced seismicity hazard (shaking intensity) (Bommer, 2022). Induced seismicity risk (the resulting damage) also increases with the proximity to densely

populated urban and coastal areas (Schultz et al., 2021). Third, knowledge of the spatial and temporal evolution of fault slip potential allows for optimizing the storage capacity using well placement and injection schedules (Hill et al., 2024). Fourth, hydraulic and mechanical properties of subsurface structures, particularly, those of faults are uncertain to varying degrees because of our limited knowledge of the subsurface (Walsh and Zoback, 2016; Kivi et al., 2023). The existing tools, which commonly rely on deterministic models, fail to fully resolve such uncertainties in their storage resource estimates. Thus, more accurate estimates of the storage capacity warrant a more robust approach to quantify fault interactions with reservoir pressurization under subsurface uncertainties.

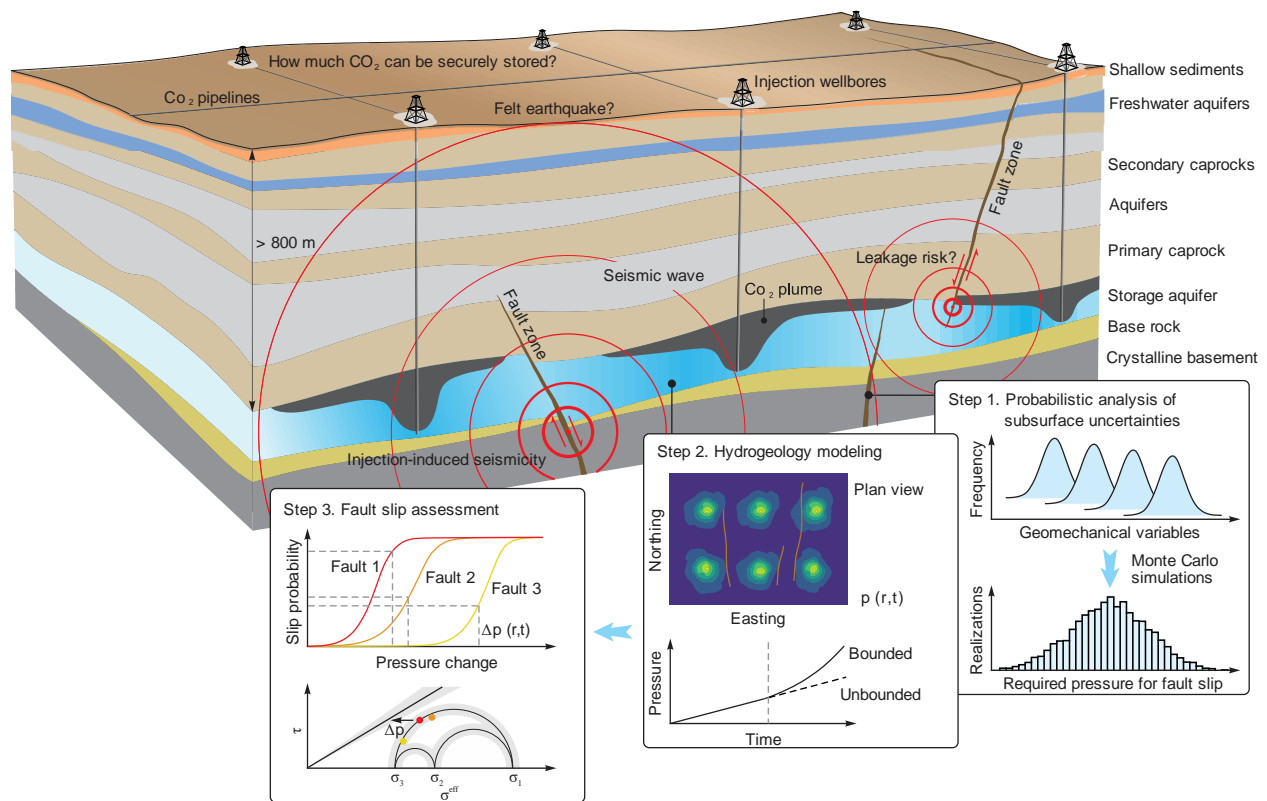


Fig. 1. Schematic illustration of basin-wide geologic CO₂ storage and constraints imposed by fault slip on the amount of CO₂ that can be securely stored underground. The inset plots show an overview of the proposed methodology for the assessment of fault slip potential.

In this study, we develop an approach using simplified physics models to estimate the impact of fault slip potential on the subsurface CO₂ storage capacity (Fig. 1). This methodology extends the tool CO2BLOCK, which estimates and optimizes storage capacity subject to reservoir injectivity limitations (De Simone et al., 2019; De Simone and Krevor, 2021). We implement the approach within an open-source and publicly available Matlab-based code, named CO2BLOCKSEISM. The tool develops a probabilistic approach to quantify fault slip probability from uncertainties in the geomechanical properties of the subsurface. It explores different injection scenarios over a range of injection site numbers and spacings to identify the maximum storage capacity subject to a specified probability of inducing felt earthquakes. We demonstrate the developed methodology against seismic activity driven by massive wastewater disposal in Oklahoma, US, in the 2010s. Extensive data are available in this region. We also apply the tool to study CO₂ storage capacity constrained by the evolution of fault slip potential in the Southern Utsira Unit in the North Sea. The tool will provide further realism to resource assessment for CO₂ storage through the incorporation of a leading physical constraint that has previously been absent from the estimates.

2. Methodology

We consider regional CO₂ injection through n sites into a homogeneous, isotropic saline aquifer represented by a circular cross-section of area A . The injection sites can be distributed arbitrarily to co-locate injection sites with large stationary CO₂ sources or to take into account any other operational, economic or regulatory factors (see the validation study in Section 3). In the absence of data to constrain injection site distribution, we consider regular distributions on rectangular grids equally spaced at distance d in either $m \times m$ or $m \times (m+1)$ configurations. We

assume different possible injection scenarios by changing the parameters n (and equivalently m) and d , limited by the areal extent of the reservoir through

$$d \leq \sqrt{\frac{A}{n}}. \quad (1)$$

The tool comprises two main modules: (1) a deterministic hydrogeology model that employs analytical solutions to calculate pore pressure evolution over space and time and (2) a probabilistic fault slip model that uses the Monte Carlo scheme to propagate uncertainties in the subsurface through the calculations of fault slip tendency (Fig. 1). The hydrogeology model is applied to all injection scenarios while the fault slip model is independent of injection conditions and implemented only once. Integration of the two modules returns the temporal evolution of slip probability along each of the mapped faults or fault segments in the region of interest. We also roughly estimate the magnitudes of nucleated seismic events, providing a physically sound criterion to constrain storage resource estimates. Explanations of these calculations are detailed below.

2.1. Reservoir pressure response to multi-site CO₂ injection

We here adapt the analytical solution developed by Nordbotten et al. (2005) for the two-phase flow of CO₂ and brine around a single wellbore injecting CO₂ at a constant rate into an infinite, homogeneous, horizontal aquifer of constant thickness. The injection is assumed to be uniform across the entire height of the reservoir. Assuming vertical equilibrium due to fast CO₂ gravity override, constant fluid densities and viscosities for each phase and a sharp CO₂-brine interface with each side of the interface fully saturated with the respective fluid, closed-form expressions for vertically averaged pressure build-up are derived for three reservoir regions: (1) adjacent to the wellbore, fully saturated by CO₂, (2) far-field, fully saturated by brine, and (3)

transition region where the two fluids coexist (Nordbotten et al., 2005; Vilarrasa et al., 2010; Huang et al., 2014). This solution can be further simplified by replacing the transition zone with a fictitious equivalent vertical interface, which yields (De Simone et al., 2019)

$$\Delta p(r, t) = \frac{Q\mu_b}{2\pi kH\rho_c} \times \Delta p^*(t, r), \quad (2)$$

where

$$\Delta p^*(t, r) = \begin{cases} \frac{\mu_c}{\mu_b} \ln\left(\frac{\psi}{r}\right) + \ln\left(\frac{R}{\psi}\right) & , r \leq \psi \\ \ln\left(\frac{R}{r}\right) & , \psi < r \leq R \\ 0 & , R < r. \end{cases} \quad (3)$$

In these expressions, $\Delta p(r, t)$ is pressure change at time t and distance r from the wellbore, Q is the mass flow rate, k is the absolute reservoir permeability, H is the reservoir thickness, ρ_c is the average CO₂ density across the plume, μ_b and μ_c are average brine and CO₂ dynamic viscosities, respectively, $R = \sqrt{2.25kt/(\mu_b(c_r + \phi c_b))}$ is the radius of influence to which pressure diffusion propagates at time t , ϕ is the rock porosity, c_r and c_b are rock and brine compressibilities, respectively, and ψ is the radius of the fictitious equivalent vertical interface and writes

$$\psi = \xi e^\theta, \quad (4)$$

where $\xi = \sqrt{Qt/(\pi\phi H\rho_c)}$ is the extent of advective propagation of the cylindrical CO₂ front and $\theta = (\mu_c + \mu_b)/(\mu_c - \mu_b) \ln(\sqrt{\mu_c/\mu_b}) - 1$ represents a function of fluid mobilities. An underlying assumption is that the radius of influence is always ahead of the CO₂ plume, which is the case in most realistic scenarios. If this condition is not satisfied, the portion of the domain affected by pressure variation is completely saturated in CO₂, and the solution is simply given by

$$\Delta p^*(t, r) = \frac{\mu_c}{\mu_b} \ln\left(\frac{R}{r}\right). \quad (5)$$

The performance of this simplified solution has been verified against numerical simulations (De Simone et al., 2019). Pore pressure varies logarithmically with distance from the injection wellbore. Thus, plotting pore pressure versus the logarithm of distance results in a bilinear curve with a sharp shift in the slope as a result of the fluid viscosity change at $r = \psi$. The original Nordbotten et al. (2005) solution returns the same estimates of pore pressure in the near-wellbore and far-field but slightly different in the transition zone as fluid viscosity is represented by a linear weighted averaging of those of brine and CO₂. We here use the compacted version of the solution (De Simone et al., 2019) as it enables calculations in a straightforward manner, particularly, for time-varying injection rate scenarios explained below.

The solution for constant-rate injection into an infinite reservoir (Eqs. 2-5) can be extended to a multi-rate injection schedule assuming that the superposition principle (in the time domain) is valid for the two-phase flow (Zimmerman, 2018)

$$\Delta p(r, t) = \frac{Q_0 \mu_b}{2\pi k H \rho_c} \times \Delta p^*(t, r) + \sum_{i=1}^{i=N} \frac{(Q_i - Q_{i-1}) \mu_b}{2\pi k H \rho_c} \times \Delta p^*(t - t_i, r), \quad (6)$$

where Q_0 denotes the initial injection rate and Q_i is the injection rate beginning at time t_i . The injected CO₂ volume for calculation of ξ in Eq. (4) also needs to sum over all injection steps until time t .

In the case of multi-site injection into an aquifer, pressure build-up at any location can be estimated by applying the superposition principle in the space domain. To this end, single-site calculations in Eqs. 2-6 are repeated for each site considering the respective distances and injection rates, and superimposed to yield pressure change at each point. Using the superposition principle

in space for a two-phase flow regime incurs an error increasing with the number of injection sites, because the increased mobility around each of the other injectors is ignored (De Simone et al., 2019). However, the error leads to systematic overestimation of the pressure build-up, and will lead to conservative estimates of fault slip potential.

2.2. Fault slip potential

We adopt the linear Coulomb faulting theory to determine whether a planar fault undergoes slip in response to injection,

$$\tau > \mu \sigma'_n. \quad (7)$$

A fault begins to slip when the shear stress τ projected onto the fault plane overcomes the frictional strength governed by the constant friction coefficient μ and the effective normal stress $\sigma'_n = \sigma_n - p$ that clamps the fault. Injection-induced perturbations in the stress field, pore pressure or fault strength can push the fault toward failure conditions. Postulating that direct diffusive pressure build-up operates as the primary mechanism of fault reactivation (Ellsworth, 2013; Ge and Saar, 2022; De Simone et al., 2023), the critical overpressure Δp_{cr} to initiate fault rupture can be obtained from rearranging Eq (7),

$$\Delta p_{cr} = \sigma_n - p - \frac{\tau}{\mu}, \quad (8)$$

where all terms on the right-hand side of the equation refer to the preinjection state of the parameters. Hence, fault stability depends on the magnitude and direction of in situ stress components, pore pressure, friction coefficient and the orientation of the faults. In practice, these parameters involve uncertainties to varying degrees, from pore pressure and some components of the stress tensor that can be directly measured at the location of the injection sites to fault attributes

and frictional strength, which are commonly less well constrained (Healy and Hicks, 2022; Kivi et al., 2023; Xiang et al., 2024). We use a statistical approach based on Monte Carlo simulations to incorporate these uncertainties into the determination of fault slip potential.

We describe uncertainties in input variables of the fault slip model using specified probability distribution functions. We use normal (or Gaussian) distributions except for pore pressure and fault dip, which are represented by uniform and truncated normal distributions, respectively. The Monte Carlo simulations repeatedly draw random samples from the data pools of input variables and calculate from Eq. (8) the required pressure for fault slip for each of these realizations. The number of realizations needs to be large enough to generate statistically representative distributions reflecting uncertainty in the critical pressure build-up for each fault (segment). We consider 5000 realizations in the examples presented in this study although the resulting distributions become almost insensitive to the number of realizations larger than a few hundred. We calculate for each of the generated distributions of critical slip pressure the cumulative distribution functions (CDF), which represent the probability of slip as a function of pressure changes on each fault. It is then straightforward to find from these curves the slip probability corresponding to time-varying estimates of the overpressure for each fault (obtained from the deterministic hydrogeologic model in Section 2.1). In this way, we infer the evolution of fault slip probability across the basin and over the injection lifetime.

It should be noted that the term probability here is reflective of the considered uncertainties but does not include other fault rupture complexities that may be important, e.g., the influence of small-scale heterogeneities in fault geometry, material properties and locally-resolved stresses (Walsh and Zoback, 2016; Hennings et al., 2019; Healy and Hicks, 2022). Therefore, the calculated values may differ from the real probability of fault slip. Indeed, they should rather be viewed in a

relative way for screening which faults are more (or less) prone to slip or in which injection scenarios or periods fault slip is more likely to happen.

2.3. Induced seismicity magnitude

Optimizing CO₂ storage capacity requires a comparison between different injection scenarios in terms of the evolution of fault slip probability calculated in Section 2.2. Such a comparison may be challenging because of the vast area of interest and number of faults that are affected by injection. Furthermore, not all fault slips are problematic as they may only induce low-magnitude events. Therefore, we should define appropriate objective functions that capture spatial variations of fault slip probability and account for the (seismic) risk and hazard they may pose. We choose to minimize the number and maximum occurrence probability of induced earthquakes exceeding certain magnitude thresholds. Assessment of these criteria is subject to estimation of possible earthquake magnitudes following fault slip.

We calculate the moment magnitude M_w using the standard relation (Kanamori and Anderson, 1975),

$$M_w = \frac{2}{3} \log_{10} M_0 - 6.07, \quad (9)$$

where M_0 is the seismic moment in N m. Assuming that the fault rupture area has a circular shape, the seismic moment can be estimated following Eshelby (1957),

$$M_0 = \frac{16}{7} r_0^3 \Delta\sigma, \quad (10)$$

where $\Delta\sigma$ is the shear stress drop as a result of slip and r_0 is the radius of the rupture area. The rupture geometry is highly uncertain because it is always unknown what portion of the total length of a fault or fault segment undergoes dynamic rupture in a single event. We make the conservative

assumption that rupture takes place fully seismically and over the full length of the fault (segment). The shear stress drop is also estimated to fall in a wide range from 1 to 10 MPa for tectonic earthquakes (Kanamori and Brodsky, 2004). It is broadly accepted that stress drops associated with small- and moderate-sized earthquakes ($M_w < 6$), including induced events, tend toward the lower bound of the range with a representative value of $\Delta\sigma = 1$ MPa (Eq. 10) as we also adopt in this study (Abercrombie, 2021; Langenbruch et al., 2024).

2.4. Validation study in Oklahoma, USA

2.4.1. Induced seismicity in central to north Oklahoma

The central and eastern United States began to experience a dramatic rise in the number of small- to moderate-sized earthquakes since 2009 (Ellsworth, 2013). The earthquakes are found to be strongly linked in time and space with wastewater disposal by injection into the subsurface (Weingarten et al., 2015). The wastewater has mostly originated from saline water co-produced with oil or backflow of hydraulic fracturing of shale gas resources. The observed correlations among other lines of evidence suggest that this unprecedented seismicity has most likely been induced.

Induced seismicity escalated in Oklahoma more than any other state in the US. Thousands of felt $M_w \geq 3$ earthquakes occurred in central to north Oklahoma and southernmost Kansas, which were seismically quiet before 2009. The seismic activity was broadly associated with massive wastewater disposal into the basal sedimentary Arbuckle Group (Keranen et al., 2014; Walsh and Zoback, 2015). However, the majority of earthquakes occurred at a depth range of 2 to 6 km below

the injection intervals in the critically stressed crystalline basement (Schoenball and Ellsworth, 2017; see Section S1 in Supplementary Information for the concept of critically stressed crust).

The frequency of felt earthquakes jumped in 2013 and reached a peak in 2015 in response to a marked increase of more than 3 folds in the injection rates (Fig. 2). Following regulations for regional reduction of injection rates in early 2016, the number of felt earthquakes declined rapidly (Oklahoma Corporation Commission, 2016). Seismicity rate response to either injection rate increase or decrease features time lags of several months (Fig. 2). This delay is in agreement with characteristic times of pore pressure diffusion along basement-rooted faults down to seismogenic depths (Langenbruch and Zoback, 2016; Raza et al., 2023). It is also well recognized that pressure perturbations continue to propagate far away from the injection sites even after injection reduction or cessation and possibly reactivate distant faults depending on their propensity to slip (Healy et al., 1968; Kivi et al., 2024). As a result, three $M \geq 5$ earthquakes, including the 2016 Pawnee $M = 5.8$ event — the largest earthquake ever recorded in Oklahoma — were induced after the mandated large-scale injection reductions (Fig. 2). Regional assessment of slip probability of known faults could contribute to lowering induced earthquake hazard.

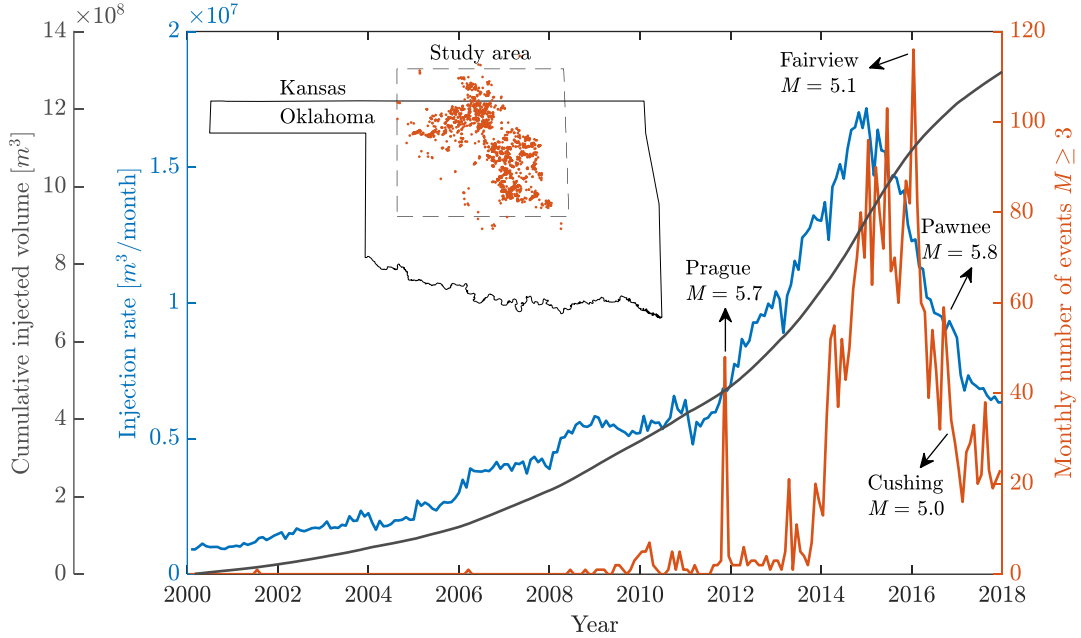


Fig. 2. Wastewater disposal and induced seismicity in Oklahoma and Southern Kansas. Variation with time of total monthly injection rate (blue), monthly frequency of $M \geq 3$ earthquakes (orange) and cumulative injected wastewater volume (grey) from Jan 2000 through Dec 2017. The inset shows the study area with the distribution of $M \geq 3$ earthquakes through Dec 2017 shown in orange dots. Injection rate data are from Norbeck and Rubinstein (2018) and seismicity data from USGS (2024).

Nearly 1.3 Gt of wastewater was cumulatively injected in less than two decades into the subsurface in central to north Oklahoma (Fig. 2). The scale of injection is comparable to that projected for large-scale CCS in saline aquifers. Thus, the recorded seismicity data in Oklahoma offers a unique opportunity to demonstrate the developed approach for estimating fault slip potential at the basin scale, the focus of our application. It is worth noting that we only analyze fault slip potential at the end of injection. Detailed assessment of the temporal evolution of

subsurface response to fluid injection in this problem requires several assumptions regarding structural and flow parameters and hydromechanical properties of faults in the crystalline basement, where ruptures took place (Langenbruch et al., 2018; Norbeck and Rubinstein, 2018). Numerical simulations should be developed to capture these complexities. Also note that the problem is single-phase as only brine is injected; thus solution for pressure build-up (Eqs. 2-6) simplifies.

2.4.2. Model parameterization

We consider a square-shaped model domain with an edge length of 300 km extended from the southwest corner at 35.2° N 99.5° W. The target storage formation, the Arbuckle Dolomite, is assumed to have a uniform thickness of $H = 400$ m with its top residing at a depth of $D = 2100$ m (Hovorka et al., 2012). We discretize the time domain to monthly intervals and the space to 40,000 equally-sized grids for which pressure changes will be calculated (Eqs. 2-6). Open flow lateral boundary conditions are used, justified by the large lateral extent of the Arbuckle Formation and field observation of low-pressure injections; injections were either gravity-driven or required small wellhead pressure within the range of frictional pressure drop along the wellbores (Langenbruch et al., 2018).

Observations of low-pressure injections justify the use of a high reservoir permeability of $k = 10^{-12}$ m², representing the upper bound of the reported permeability range for Arbuckle Dolomite (Morgan and Murray, 2015). We consider formation porosity and bulk compressibility of $\phi = 0.2$ and $c_r = 0.16 \times 10^{-10}$ Pa⁻¹, respectively, measured from laboratory experiments and back-analysis of field observations (Kroll et al., 2017; Langenbruch et al., 2018). Considering reservoir temperature of 50°C and brine salinity of 100,000 ppm, formation brine has compressibility and

dynamic viscosity of $c_b = 4.4 \times 10^{-10} \text{ Pa}^{-1}$ and $\mu_b = 5.5 \times 10^{-4} \text{ Pa.s}$, respectively (Hovorka et al., 2012).

A summary of fluid and rock properties is provided in Table 1.

Table 1. Summary of parameters used in hydrogeologic modeling of wastewater disposal in Oklahoma, US, and CO₂ injection at Utsira storage unit, Norway.

Parameter	Wastewater disposal	CO ₂ storage
	Oklahoma, US	Utsira Formation, Norway
Reservoir top depth, D [m]	2100	900
Reservoir thickness, H [m]	400	250
Permeability, k [m ²]	10^{-12}	10^{-12}
Porosity, ϕ [-]	0.2	0.35
Bulk rock compressibility, c_r [Pa ⁻¹]	0.16×10^{-10}	3.4×10^{-9}
Brine compressibility, c_b [Pa ⁻¹]	4.4×10^{-10}	4.1×10^{-10}
Brine viscosity, μ_b [Pa.s]	5.5×10^{-5}	8.2×10^{-4}
CO ₂ density, ρ_c [kg/m ³]	-	Equation of state
CO ₂ viscosity, μ_c [Pa.s]	-	Equation of state

We construct our hydrogeologic model of the study area based on the saltwater disposal database compiled by Norbeck and Rubinstein (2018). The database documents monthly injection rates of 875 wells in central to north Oklahoma and southernmost Kansas from Jan 2000 through Dec 2017. The distribution of injection wellbores and the cumulative injected fluid volume for each wellbore are illustrated in Fig. 3a. We extract seismicity data in the same period from the ANSS Comprehensive Earthquake Catalog (ComCat) (USGS, 2024).

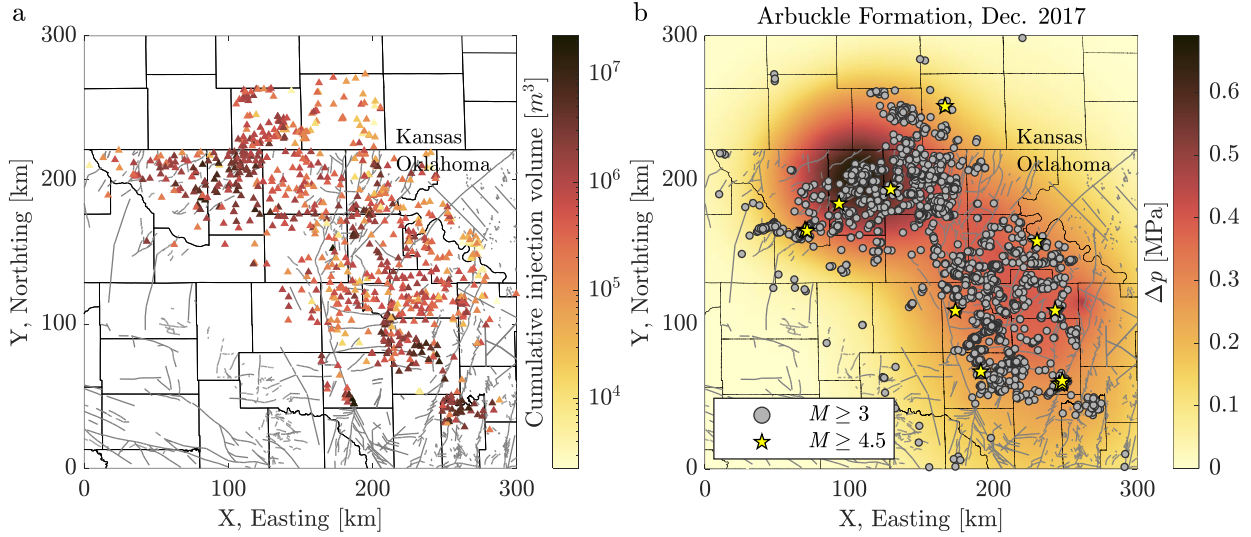


Fig. 3. Spatial correlation between wastewater disposal and induced seismicity. (a) distribution of wastewater disposal wells, color-coded with the cumulative injected fluid volume in the period from Jan 2000 to Dec 2017 (data from Norbeck and Rubinstein, 2018) and (b) distribution of injection-induced pore pressure build-up (estimated and discussed in Section 3.1) and seismic events ($M_w \geq 3$ grey circles, $M_w \geq 4.5$ yellow stars) through Dec 2017 (data from USGS, 2024). Grey lines in the background show mapped faults in the sedimentary layers.

We use available data from the literature to constrain the state of stress in the subsurface (Table 2, Fig. S2). We exclude any information obtained from the interpretation of induced seismicity data as we primarily aim to demonstrate the capability of the developed tool for fault slip analysis at a screening level prior to injection operations. In particular, inversion of focal plane mechanisms associated with induced seismic events has been used to constrain the orientation and relative magnitude (stress regime) of stress components in the study area (Alt and Zoback, 2016; Walsh and Zoback, 2016). The gained insights imply a transition of stress regime from strike-slip regime ($\sigma_{Hmax} > \sigma_v > \sigma_{hmin}$, where stress terms from the left denote maximum horizontal stress,

vertical stress and minimum horizontal stress, respectively) in central Oklahoma to normal regime ($\sigma_v \geq \sigma_{Hmax} > \sigma_{hmin}$) in north Oklahoma with slight rotations of the σ_{Hmax} orientation. However, we disregard this *post-facto* information and assume a uniform stress distribution characterized by strike-slip faulting and a σ_{Hmax} orientation of N80°–90°E with an average of N85°E, as inferred from wellbore tensile fracture and shear breakout data (Alt and Zoback, 2016; Heidbach et al., 2018).

We assume an average vertical stress (σ_v) gradient of 25 MPa/km corresponding to a typical overburden rock density of 2500 kg/m³. Initial pore pressure, p , is assumed to be sub-hydrostatic and assigned a uniform distribution with an average gradient of 9.6 MPa/km. We constrain horizontal stress magnitudes, considering the frictional strength of the Earth's crust (see Section S1 in Supplementary Information for a detailed explanation). In the absence of wellbore measurements to estimate stress magnitudes or to narrow down possible ranges, the resulting distributions of horizontal stress components involve large uncertainties (Fig. S2).

We calculate stress components and pore pressure for a depth of 2500 m, i.e., the top of the crystalline basement, hydraulically connected to the storage formation. This is because the seismogenic depth range is a priori unknown but one could anticipate more seismic activity in the crystalline basement as it is commonly more critically-stressed than the overlying sediments (Kivi et al., 2023).

We retrieve fault information, including centroid coordinate and strike of fault segments, from the Oklahoma fault database compiled from petroleum industry data and published literature (Darold and Holland, 2015). The database is mainly sourced from seismic and well data in sedimentary formations and may obviously miss faults in the crystalline basement if they are not

extended enough upward into the sedimentary cover. Our model domain includes a total of 7480 fault segments for which stability analysis is separately performed.

In the absence of information about the fault dip, we assume sub-vertical faults, favoring slip under strike-slip stress conditions. This is supported by the association of low-pressure injection leading to seismic activity in the study area (Langenbruch et al., 2018). We add Gaussian noise to the mapped fault strikes to account for possible measurement uncertainties and non-planar fault geometries. The fault friction, μ , is also represented by a Gaussian distribution with an average and standard deviation of 0.6 and 0.03, respectively, consistent with laboratory measurements (Bayerlee, 1978) and field observations (Barton et al., 1995) for faults crossing crystalline rocks. Distributions of fault parameters are summarized in Table 2 and illustrated in Fig. S2.

Table 2. Statistical distributions of input variables used for the analysis of fault slip potential in Oklahoma, the US, and the Utsira storage unit, Norway discussed in Section 2.5.

Parameter	Wastewater disposal			CO ₂ storage		
	Oklahoma, the US			Utsira Formation, Norway		
	Distribution	Mean	Standard deviation	Distribution	Mean	Standard deviation
p gradient [MPa/km]	Uniform	9.6	0.6	Uniform	10.2	0.2
σ_v gradient [MPa/km]	Gaussian	25	0.5	Gaussian	21	0.2
σ_h gradient [MPa/km]	Gaussian	20	1	Gaussian	17	1
σ_H gradient [MPa/km]	Stress criticality	Calculated	Calculated	Gaussian	19	0.1

σ_H orientation [°]	Gaussian	85	1.5	Gaussian	100	10
Fault strike [°]	From map	variable	2	From map	Variable	2
Fault dip [°]	Truncated	90	5	Truncated	55.5	18
	Gaussian			Gaussian		
μ [-]	Normal	0.6	0.03	Normal	0.38	0.03

2.5. Application to resource assessment in the Utsira Formation, Norway

2.5.1. Geological setting

We demonstrate the application of the developed tool to estimate the CO₂ storage resource constrained by fault slip potential in the Utsira Formation. The Utsira is the unit for the first dedicated CO₂ storage project and it is one of the largest saline aquifers in the Norwegian sector of the North Sea. The formation is mainly composed of sand and extends nearly 450 km N-S and 90 km E-W (Fig. 4; Halland et al., 2014). The large extent, estimated storage resource, and injectivity of this unit make it an attractive target for large-scale CO₂ storage (Gasda et al., 2017; Elenius et al., 2018; Pettersson et al., 2022). Since 1996, nearly one megatonne of CO₂ from the Sleipner Field has been annually injected into this formation. Estimates of storage capacity subject to caprock integrity point to huge potential for scaling up CCS in the Utsira Sand to several gigatonnes (Lindeberg et al., 2009; Gasda et al., 2017).

The Utsira Formation regionally dips upward toward the west (Fig. 4). The depth of the formation top ranges from 1000 m in the north to around 200 m in the west. These topographical variations render the southern and northern portions of the formation suitable for CO₂ storage. Our study focuses on the southern region where the formation has a larger thickness, locally exceeding

300 m. Our region of interest has a square shape with an edge length of 120 km extended from the southwest corner at 57.90° N 1.34° W. We represent the southern Utsira unit with a fictitious square-shaped boundary of equivalent areal extent located at the center of the model domain to set a reference for considering different injection scenarios. Injection site configurations are deemed admissible only if they fully reside in this equivalent boundary. More than 50 years of petroleum exploration and exploitation activity have enriched data on subsurface structures and properties in this area, including the distribution of the faults, which we use in this study (Fig. 4).

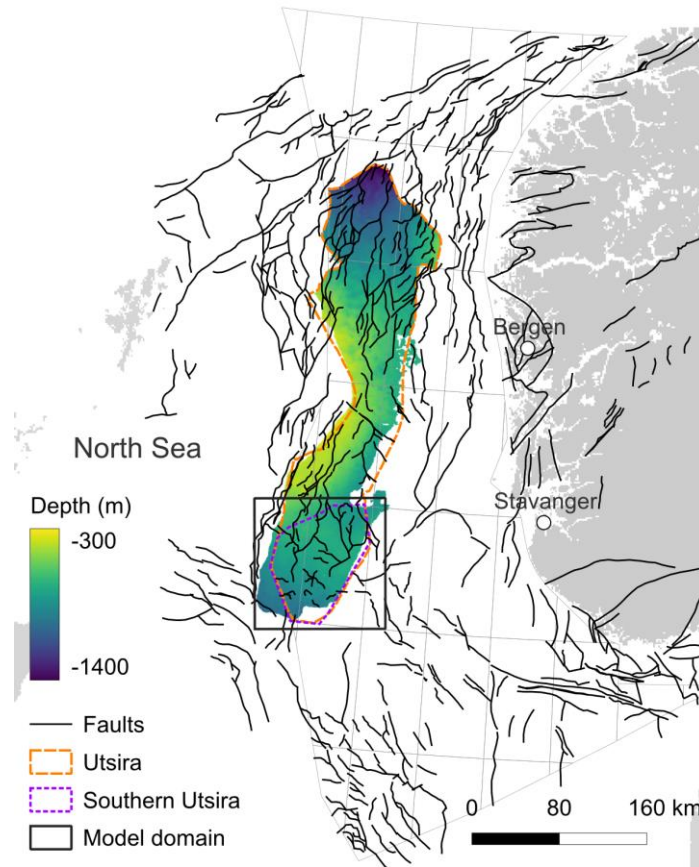


Fig. 4. Study area with the depth map of the Utsira Formation top. Dashed orange and purple lines illustrate the extent of the Utsira Formation and the southern Utsira region, respectively. The black square represents the model domain. Sparse black lines show the mapped faults.

2.5.2. Model parameterization

All model parameters are derived for a depth of $D = 900$ m below sea level including 117 m water depth (Kirby et al., 2001). This depth stands at the top of the Utsira Formation where fault reactivation could compromise the caprock integrity. We consider an average reservoir thickness of $H = 250$ m for the southern Utsira Formation (Gasda et al., 2017). We assume a formation porosity of $\phi = 0.35$ and permeability of $k = 1 \times 10^{-12}$ m², which represent the mean values inferred from laboratory measurements and wellbore-scale analyses at the Sleipner CO₂ storage site (Zweigel et al., 2004).

The reservoir has a temperature of 35°C and brine salinity of 35,000 ppm (Zweigel et al., 2004), which result in brine compressibility and dynamic viscosity of $c_b = 4.1 \times 10^{-10}$ Pa⁻¹ and $\mu_b = 8.2 \times 10^{-4}$ Pa.s, respectively. The Utsira Sand has a bulk compressibility of $c_r = 3.4 \times 10^{-9}$ Pa⁻¹, which is higher by nearly one order of magnitude than typical sandstone compressibilities (Gasda et al., 2017). The density (ρ_c) and dynamic viscosity (μ_c) of CO₂ are calculated from Equations of State (EOS) proposed by Spycher et al. (2003) and Altunin and Sakhabetdinov (1972), respectively. Adopting these fluid and rock properties (see Table 1 for a summary), we perform pressure calculations in response to CO₂ injection at a constant rate of $Q = 10$ Mt/y per site over 40,000 grids of the model domain and yearly time intervals (Eqs. 2-5). The large lateral extent of the Utsira justifies the assumption of open flow boundary conditions.

We parameterize statistical distributions of the geomechanical variables required for slip analysis using data from the literature (Table 2, Fig. S3). We assume a normal faulting stress regime, which is the prevailing conditions in offshore areas and also agrees with measurements reported in the World Stress Map (Heidbach et al., 2018). Measurements of the σ_{Hmax} orientation

show an average of N100°E with a maximum uncertainty of $\pm 25^\circ$ (Heidbach et al., 2018). The overburden stress, σ_v , varies with depth from the sea floor at an average gradient of 21 MPa/km, calculated from a density of 2100 kg/m³ assumed for the overlying layer, i.e., the Nordland Shale. The initial pore pressure, p , is assumed to be hydrostatic, corresponding to an average gradient of 10.2 MPa/km. The minimum horizontal stress, σ_{hmin} , follows a gradient of 17 ± 3 MPa/km fitted on leak-off pressure data in the study area (Elenius et al., 2018). In the absence of measurements for the maximum horizontal stress, σ_{Hmax} , we assume that it lies in the middle of the range between the two other stress components.

The fault information is accessible from the interactive CO₂ atlases of the Norwegian Continental Shelf (Norwegian Offshore Directorate, 2015). The model domain covers 1400 fault segments, which are assumed to cross the reservoir. We approximate the fault frictional strength using an empirical correlation between the friction angle, φ , and porosity, ϕ , established from a large dataset of measurements on unconsolidated sands (Weingarten and Perkins, 1995),

$$\varphi = 57.8 - 105\phi. \quad (11)$$

Considering a porosity range of 0.3 to 0.4 for the Utsira Sand (Kirby et al., 2002), we find that the friction coefficient $\mu = \tan(\varphi)$ ranges from 0.28 to 0.49 with an average of 0.38. Laboratory experiments on a poorly cemented North Sea sandstone analogous to the Utsira Sand measure a friction coefficient of 0.35 (Park et al., 2022), which agrees well with those obtained from Eq. (11). Since the fault dip distribution is not constrained by any means, we adopt the full possible range from sub-horizontal to sub-vertical with an average value representing optimal orientation for slip, i.e., 55.5° for the average friction coefficient considered above. We generate possible ranges of fault strikes by adding Gaussian noise to the mapped values.

3. Results

3.1. Validation study against induced seismicity in Oklahoma, USA

The high permeability of the Arbuckle Formation and broad distribution of injection wellbores result in widespread pressure perturbation across the study region (Fig. 3). Pressure build-up at injection depths remains in the range of few bars and is more pronounced in north Oklahoma where high-rate injectors are closely located. The calculated pressure variations are in general agreement with those obtained numerically in other studies (see for example Fig. 1 in Langenbruch et al., 2018). We estimate broad spatial correlations between seismicity and pressure changes (Fig. 3b). This points to (1) the effective hydraulic connection between sedimentary layers and seismogenic depths in the crystalline basement and (2) the key role of pressure diffusion in inducing seismicity at large scales. There are also some regions of elevated pressure around the Oklahoma-Kansas border with no recorded felt seismicity ($M \geq 3$). This can be due to the lower density or slip propensity of faults or the presence of unresolved flow barriers preventing pressure communication with the faults in these areas.

Monte Carlo simulations of fault stability result in slip probability curves for each of the fault segments (Figs. 5 and S4). The tendency of a fault segment to slip is primarily governed by its orientation. Steeply dipping faults striking approximately N54°E or N116°E, i.e., a 31° deviation on either side of the maximum horizontal stress orientation, would be the most likely to slip. The stress criticality assumption decouples to a large extent the slip probability of such optimally-oriented fault segments from uncertainties in the state of stress. In contrast, a fault deviating from this optimal orientation may require significantly different pore pressure changes to slip depending on stress conditions. Indeed, the larger the deviatoric stress, i.e., the difference between two principal horizontal stress components under the strike-slip faulting regime, the lower

the slip tendency of poorly oriented faults. Given the high uncertainties of in situ stress in the study area, the critical pore pressure calculated for different realizations of the subsurface parameters varies widely and approaches values as large as 120 MPa for poorly oriented faults to slip (Fig. S4). Furthermore, because of the small injection-induced pressure changes compared to stress uncertainties, fault slip probabilities mainly span the lower range of possible values (< 0.5). The slip probabilities could be even smaller if evaluated at larger depths in the crystalline basement due to relatively small pressure build-up and larger stress magnitudes.

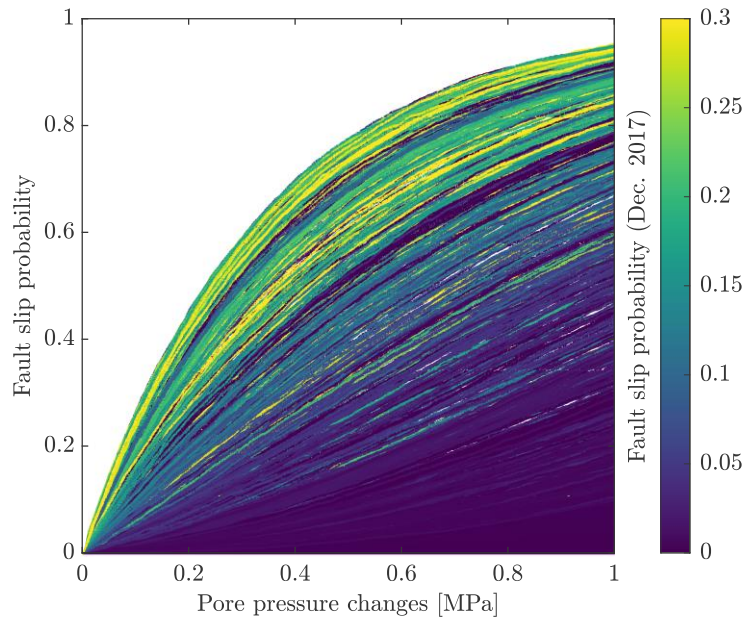


Fig. 5. Slip probability as a function of pore pressure increase for each of the fault segments in the study area, color-coded with the calculated slip probabilities at the end of the considered injection period in Dec. 2017. The color scale is adjusted to a maximum slip probability of 0.3 for visualization purposes. The slip probability curves here focus on pressure range up to 1 MPa. Those with the full range of pore pressure are presented in Fig. S4.

The developed methodology captures some features of the observed induced seismicity in Oklahoma. The low slip probability calculated for faults in the region with relatively little pressure build-up on the west of the Nemaha fault zone in central Oklahoma is consistent with the sparse seismic activity recorded in this region (Fig. 6a). We also calculate relatively high slip potential for faults ruptured by the 2011 M_w 5.7 Prague (Fig. 6b) and the 2015 M_w 4.7 Cherokee (Fig. 6c) earthquakes and the fault conjugate to the unmapped fault associated with the 2016 M_w 5.8 Pawnee event (Fig. 6e). Small changes in fault strike lead to significant variations of the fault slip potential (look at various splays of the Wilzetta fault in Fig. 6b that seemingly have identical orientations but different slip probabilities). The Prague event occurred on a splay of the Wilzetta fault zone that was not fully mapped before this sequence – the full extent of the reactivated fault was inferred from earthquake focal mechanisms (Yeck et al., 2017). Similarly, numerous earthquakes, including the 2016 M_w 5.1 Fairview and its sizable foreshock (Fig. 6d) and the 2016 M_w 5 Cushing (Fig. 6f) events, occurred on unmapped faults (or fault extensions).

The dense distribution of seismic events in north Oklahoma is not correlated with the fault map. The weak correlation observed between seismicity and fault distributions can be attributed to the inadequate resolution of the fault map and the difference between fault trends in the sedimentary cover and at seismogenic depth in the crystalline basement where the majority of earthquakes occurred. This reflects that the application of this approach is limited by our knowledge of the distribution of subsurface structures prior to injection.

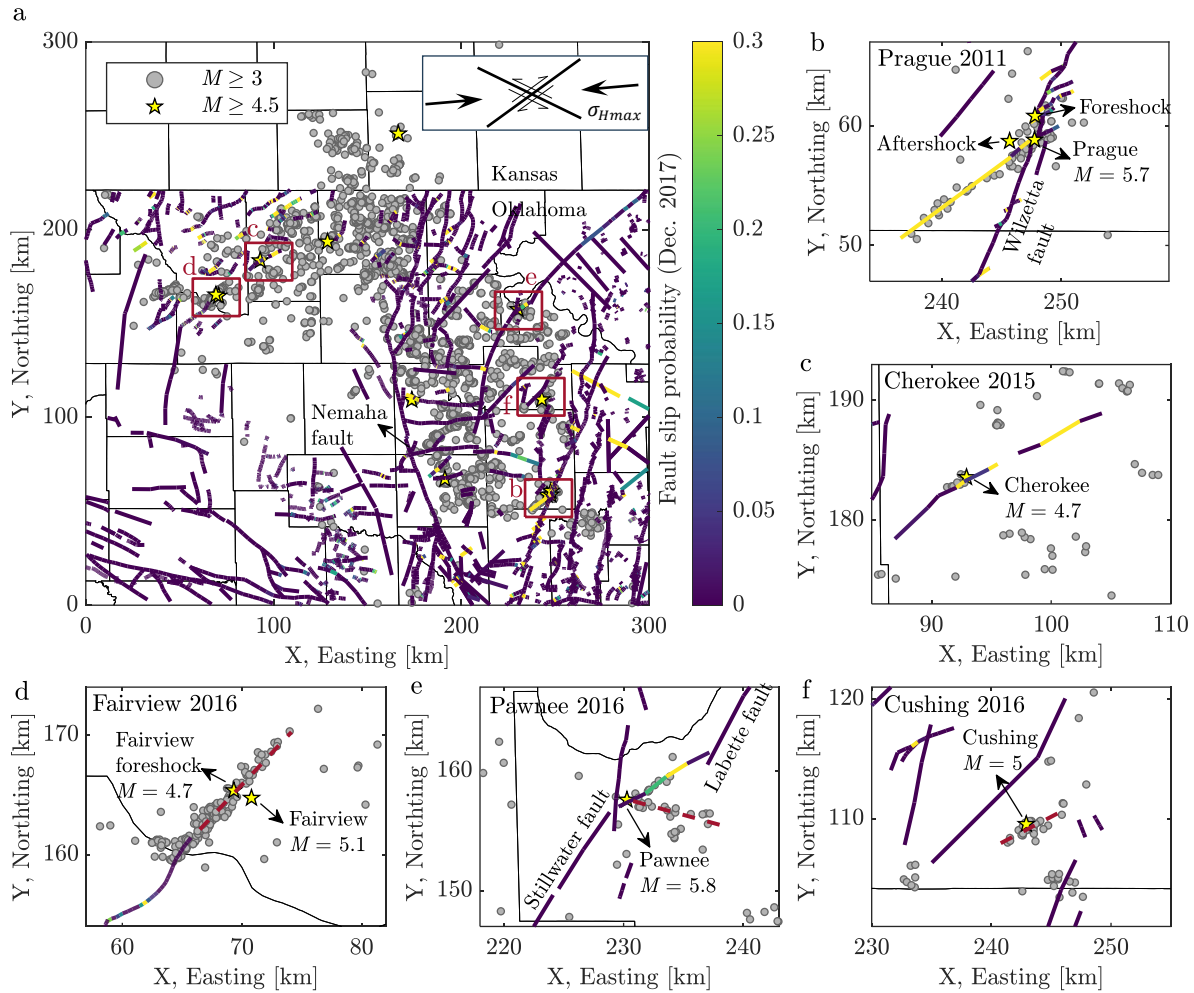


Fig. 6. Spatial distribution of fault slip probability estimated at the end of the considered injection period in Dec. 2017. Calculated slip probability of (a) all faults in the study area in the central to north Oklahoma with zoomed views of areas where the (b) 2011 Prague, (c) 2015 Cherokee, (d) 2016 Fairview, (e) 2016 Pawnee and (f) 2016 Cushing sequences ruptured. Dashed red lines in (d)-(e) show potential unmapped faults where felt earthquakes ruptured. The color scale is adjusted to a maximum calculated slip probability of 0.3 for better visualization. Recorded seismic events of $M_w \geq 3$ and $M_w \geq 4.5$ are illustrated with grey circles and yellow stars, respectively.

3.2. Storage resource assessment limited by fault slip in the Utsira Unit, Norway

3.2.1. Fault slip analysis

Slip probability for all faults in the southern Utsira storage unit follows an S-shape trend with pressure changes concentrating in a quite narrow band (Fig. 7a), i.e., there are pressure margins of 2 to 5 MPa before slip probability rapidly increases and, eventually, plateaus at the maximum value of 1. The observed trend is underpinned by the state of stress in this region, leaving some room for CO₂ injection before the faults become critically stressed. This behavior differs from that of the Oklahoma study area, where small pressure changes result in sharp increase in the slip probability of optimally-oriented faults (Fig. 4). Besides, it is observed that the required pore pressure to reactivate the faults in Utsira spans a narrower range of absolute values compared to Oklahoma obviously because of the smaller stress magnitudes at the shallower depths of investigation but also the lower uncertainties in the stress field in this region. Since the calculated pressure changes in response to long, multi-site CO₂ injection are comparable to the range of stress variations, slip probabilities grow to values close to unity (Fig. 7a).

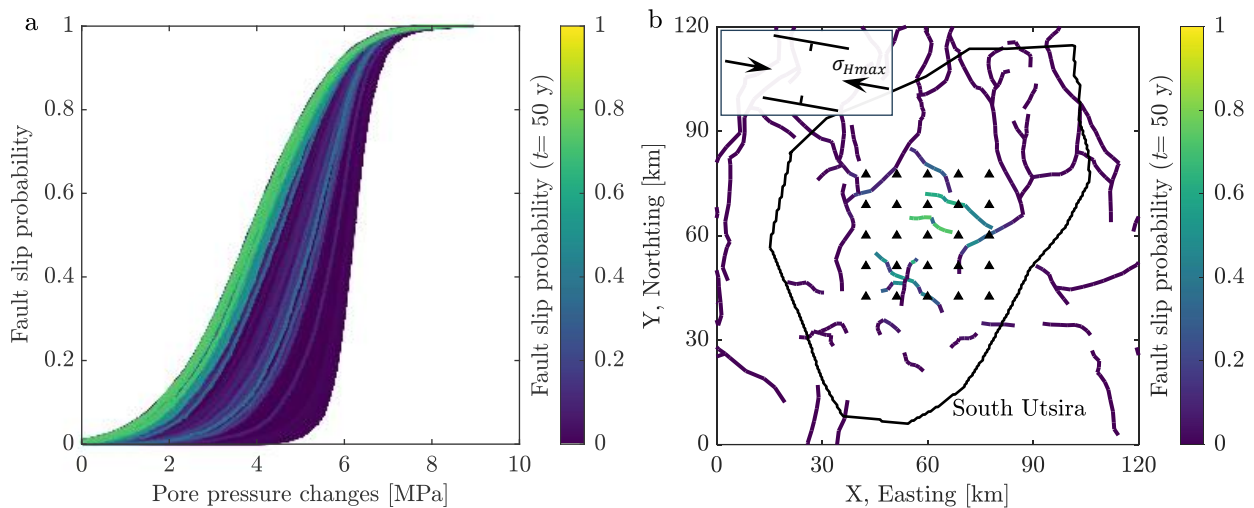


Fig. 7. Fault slip probability in the southern Utsira storage unit. (a) Slip probability curves for each of the fault segments, color-coded with its slip probability after 50 years of injection for the site configuration shown in b. (b) Spatial distribution of fault slip probability after 50 years of injection through a 5×5 array of injection sites spaced by 8.8 km and represented by triangles.

While the average dip angle is the same for all faults, the variable fault strike, controlling stress projection onto the fault planes, mainly governs the difference between slip probability curves (Fig. 7a). In particular, faults sub-perpendicular to the minimum horizontal stress undergo the largest deviatoric stress and are best oriented to slip (Fig. 7b). These faults have relatively larger slip probabilities under small overpressures and, thus, represent slip probability curves toward the left of the plot in Fig. 7a. In addition, slip probability on these faults decouples from the maximum horizontal stress and becomes a primary function of the minimum horizontal stress and the fault inclination as demonstrated by sensitivity analysis (Fig. 8). Increasing (decreasing) the minimum horizontal stress, while other parameters are maintained, shrinks (enlarges) the mohr circle (see the inset in Fig. 1) and moves the fault away from (toward) failure conditions as reflected in enhanced (decreased) critical pore pressure for fault slip. Changes in the minimum horizontal stress alter both the normal (translation of the mohr circle) and shear stress (changes in the diameter of the mohr circle) projected onto the fault plane. As a result, the slip pressure changes with the minimum horizontal stress with a factor > 1 .

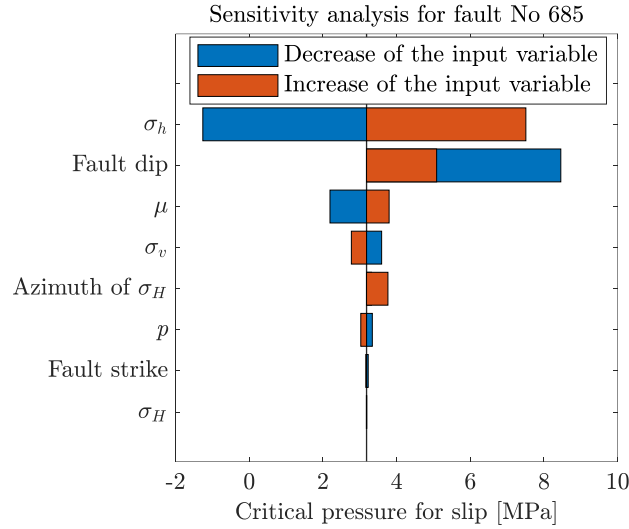


Fig. 8. Tornado plot showing relative sensitivity of critical pore pressure to different variables for an exemplary fault with optimal orientation to slip. The baseline shows the slip pressure given the average values for all variables as listed in Table 2.

The slip probability after a period of injection, is controlled by the position of the fault segments relative to the injectors, dictating spatiotemporal perturbations in pore pressure. The larger the number of injection sites and the shorter the distance between them, the larger the interference between pressure fronts and, thus, injection-induced overpressures (Fig. S5). Faults crossing the pressurized regions between the injection sites, if properly oriented, are more likely to slip (see Fig. 7b for slip probabilities after 50 years of injection). As such, seismic activity with maximum magnitudes up to 4.6 on mapped faults could be anticipated for some injection scenarios of dense site distributions resulting in pressure build-up larger than ~ 2.5 MPa (Fig. 9a). Yet, one may find properly spaced injection site configurations to significantly reduce injection overpressure and induced seismicity on the mapped faults while injecting the same amount of CO_2

(Fig. 9b). These observations highlight the importance of appropriate basin-scale injection designs to maximize injection capacity that can be safely achieved.

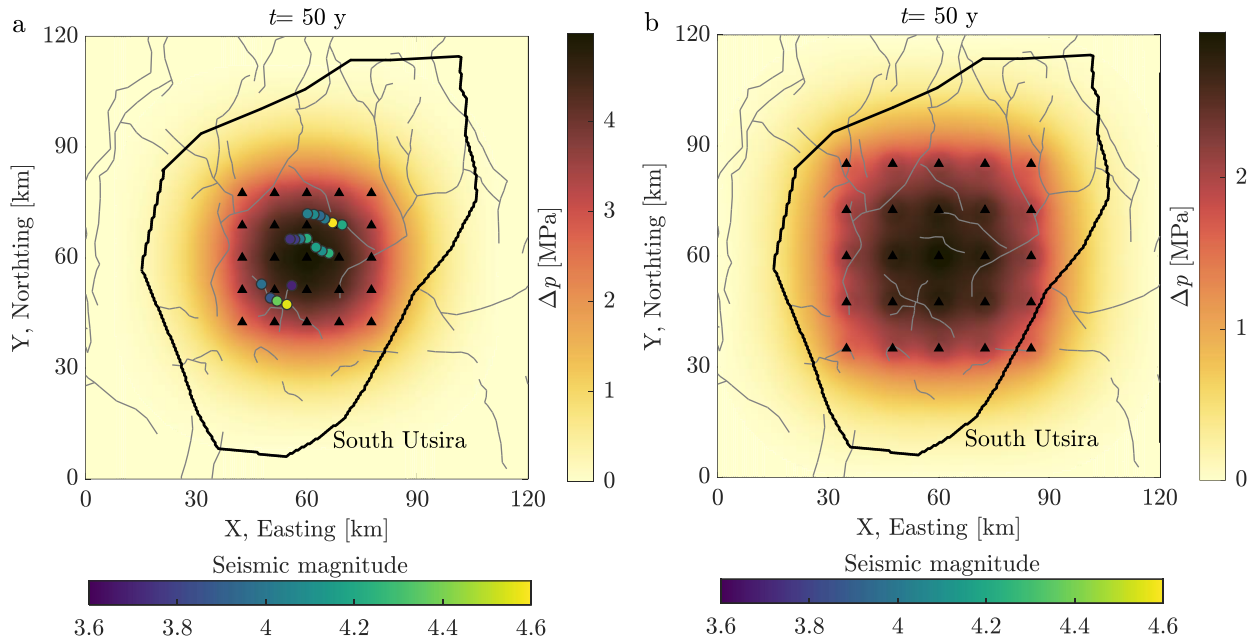


Fig. 9. Effect of injection site configurations on pressure distributions and seismic activity (events with occurrence probability $> 50\%$). (a) A dense grid of injection sites resulting in large overpressure and possibly induced earthquakes. (b) Increasing the distance between injection sites to reduce the likelihood of seismic activity on mapped faults.

The slip probability of fault segments does not evolve uniformly with time (Fig. 10). For a dense 5-by-5 grid of injectors as an example, the slip probability increases gently for more than 15 years hardly exceeding 10% for all faults. Afterwards, the likelihood of fault reactivation rises rapidly for optimally oriented fault segments while for the majority of the rest, it remains at a low level. The observed trends mimic the characteristic slip probability curves as a function of pore pressure (Fig. 7a) but also the spatiotemporal evolution of pore pressure: pore pressure increases

gently until pressure fronts of individual injection sites begin to effectively interfere and drive a rapid pressure build-up, decreasing fault stability. These results offer insights into the dynamics of storage capacity in light of the relative seismogenic behavior of the different stages of CO₂ storage.

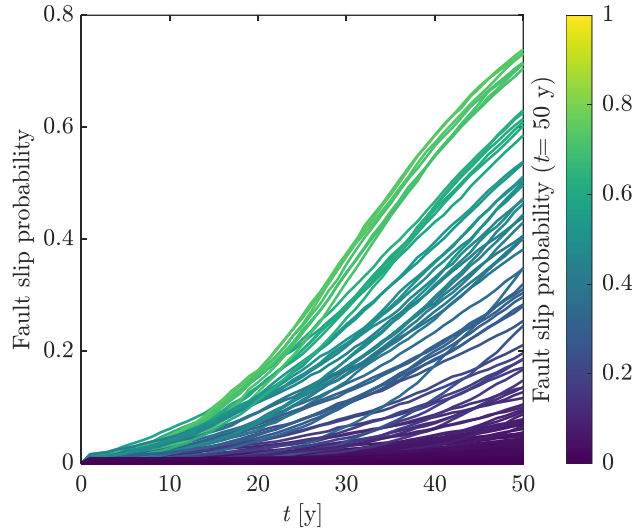


Fig. 10. Temporal evolution of fault slip probability color-coded with the slip probability after 50 years of injection through a 5×5 array of injection sites spaced by 8.8 km.

3.2.2. Storage resource assessment

We here analyze how storage capacity in Utsira is constrained by fault slip potential. We consider two criteria for relative seismic hazard assessment of different injection scenarios based on the resolved fault map: (1) maximum probability of inducing at least one event with $M_w \geq 4$ and (2) number of events with a possible magnitude $M_w \geq 4$ (events are assigned to probabilities >0.5). The magnitude 4 is selected as a threshold for an earthquake to be felt under different injection settings (Bommer and Verdon, 2024). The code CO2BLOCKSEISM evaluates these

criteria for a range of injection scenarios comprising varying numbers of injectors and allowable distances between them limited by the areal extent of the reservoir (Fig. 11).

For dense grids of injection sites spaced by either 5 or 8.8 km the probability of inducing at least one felt earthquake grows rapidly with the number of injectors (Fig. 11a). Several moderate-sized events could be anticipated for these scenarios (Fig. 11b). Increasing the distance between injection sites notably reduces both the number and probability of felt-induced earthquakes. Particularly, the calculated fault slip probabilities remain well below 10% for any possible scenario with an inter-site distance of around 16 km (Fig. 11a).

A grid of 25 injectors could safely store 12.5 Gts of CO₂ in the Utsira Formation over 50 years at a constant injection rate of 10 Mt/y. This storage capacity corresponds to approximately 3% of the initial reservoir pore volume. The injection overpressure approaches 1.7 MPa for this scenario (Fig. S6), much lower than the minimum overpressure of around 5.6 MPa for the tensile opening of sub-vertical fractures at the top of the reservoir at an average depth of 900 m given the initial pore pressure and minimum horizontal stress gradients (Table 2). Indeed, the caprock fracturing limit of 5.6 MPa corresponds to a CO₂ storage capacity of nearly 18 Gt (Fig. S6). Thus, induced seismicity, and not rock fracturing, operates as the limiting factor to CO₂ storage capacity in this region.

Our calculated storage capacity is over twice as large as previous estimates of around 5 Gts based solely on caprock integrity constraints, i.e., maximum overpressure to prevent tensile fracturing of the caprock (Lindeberg et al., 2009; Gasda et al., 2017; Pettersson et al., 2022). The difference originates from more conservative assumptions made in these studies through the application of (1) a universal maximum allowable pressure increase of 1.5 MPa as the tensile fracturing limit of the shallowest point of the caprock resolved from the reservoir topography maps

and considering a minimum horizontal stress gradient corresponding to the lower bound of field measurements from leak-off experiments (compared to our study, which parameterizes the statistical models of fault slip behavior based on the full range of stress measurements and at a depth of 900 m representing the average depth of the top of southern Utsira) and (2) fully closed boundary flow conditions (compared to our study, which considers open flow boundary conditions). According to the estimated maximum injection overpressures for different scenarios (Fig. S6), the first assumption decreases our estimate of storage capacity to nearly 8 Gts while the latter seems to be responsible for the remaining difference with that of Gasda et al. (2017) and Pettersson et al. (2022). However, the considered caprock fracturing limit of 1.5 MPa is encountered in the middle region of the formation (Fig. 4, Gasda et al., 2017), not the southern part, which is the main focus of this study. It should also be noted that the decrease in minimum horizontal stress gradient in a normal stress regime also increases the fault slip potential as it enlarges the mohr circle and brings optimally oriented faults closer to shear failure conditions (Fig. 1). Thus, we expect that the choice of input variables does not change our conclusion that induced seismicity most likely operates as the key limiting factor to the storage capacity of the Utsira Formation. CO2BLOCKSEISM can be applied with modified input data upon availability to provide more accurate estimates of storage capacity in the Utsira Formation although the demonstrated workflow remains unchanged.

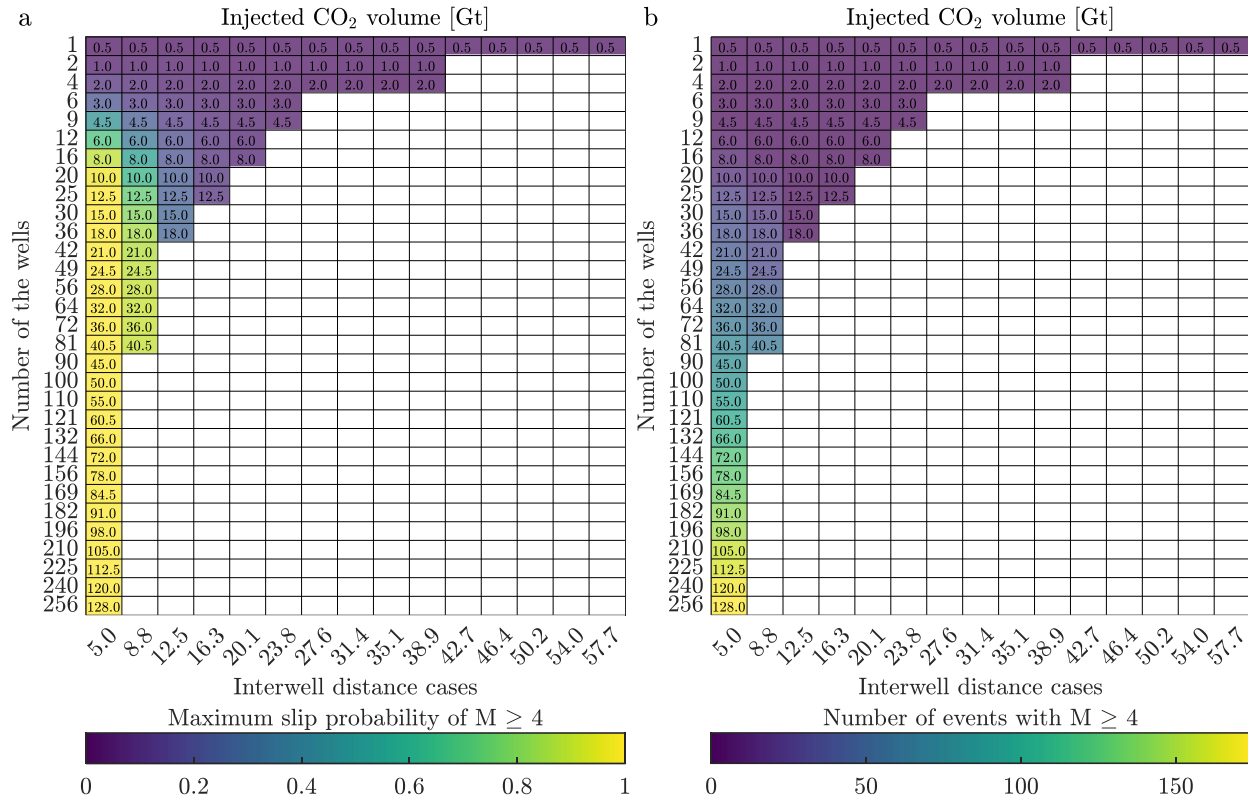


Fig. 11. Storage resource assessment constrained by fault slip potential. Storage capacities calculated for different injection scenarios and the resulting (a) maximum slip probability of $M \geq 4$ and (b) number of events with $M \geq 4$ (events with occurrence probability $> 50\%$).

4. Discussion

We have developed an analytical tool for screening subsurface CO₂ storage resources constrained by fault slip potential. We account for the spatiotemporal distribution of fault slip probability, which offers an effective criterion for comparison between different injection scenarios for regional CO₂ storage in a safe manner. However, the range of slip probabilities is affected by the level of uncertainties in geomechanical variables that could vary largely from one region to the other depending on the established knowledge of the subsurface. This difference is

evident in two distinct ranges of slip probability calculated for our case studies in Oklahoma, US, and the Utsira CO₂ storage unit in the Norwegian North Sea (compare Fig. 6 with Fig. 7). Thus, the developed methodology should not be applied for comparison between the fault reactivation or seismicity potential of projects in different geological settings.

We consider pore pressure diffusion as the primary mechanism of fault reactivation. However, several other mechanisms could contribute to fault instabilities (Ge and Saar, 2022; De Simone et al., 2023). In particular, the role of poroelastic stressing in inducing seismicity in low-pressure injections for wastewater disposal has been widely acknowledged (Goebel et al., 2017; Zhai et al., 2021). While pressure migration is still expected to adequately address fault slip potential from a broad basin-wide vision, incorporating more physical constraints into the model could improve predictions at local scales. Furthermore, we presume uniform distributions of geomechanical variables, which may not be realistic over large spatial scales of investigation. Given the availability of data from multiple sites across the storage aquifer, it would be straightforward to divide the study area into smaller regions over which the parameters can be assumed constant (Walsh and Zoback, 2016). In this way, the Monte Carlo simulations can be parameterized separately for each region, providing more accurate assessments of fault slip probability. Such model improvements should maintain the functionality of the tool for rapid, first-order screening of subsurface storage resources under existing uncertainties at the basin scale. Detailed assessment of the induced seismic hazard for optimized design of individual storage sites warrants high-fidelity numerical simulations that sufficiently capture the subsurface structural and physical complexities.

The calculated fault slip potentials do not intend to provide definitive seismic hazard maps of the study area. Significant uncertainties may arise from inaccurate and incomplete knowledge

of subsurface faults at large scales of interest to regional CCS deployment as evidenced by the majority of induced earthquakes ruptured on unmapped faults in Oklahoma (Fig. 3b). Indeed, the application of our analysis becomes limited to a priori characterization of the subsurface, which may leave many structural features in the subsurface unseen. Continuous monitoring and characterization of the subsurface during injection hold the promise of identifying potentially seismogenic faults in the subsurface and further constraining geomechanical variables (Verdon et al., 2013). The developed probabilistic approach for fault stability analysis can be employed for inverting induced (micro)seismicity observations into improved knowledge of the fault attributes and relative stress magnitudes (Walsh and Zoback, 2016; Snee and Zoback, 2018). The gathered data enables revisiting evaluations of fault slip potential. Thus, the estimated storage capacities may need to be progressively updated as complementary information from the subsurface is acquired, implying the dynamic nature of storage resource assessments.

The developed tool, CO2BLOCKSEISM, takes a step forward towards more accurate estimates of subsurface CO₂ storage resources by explicitly accounting for the spatially-variable risk of fault reactivation. Yet, it simply assumes uniform distributions of injection sites on rectangular grids injecting CO₂ at constant rates. Optimizing injection site placement and/or injection rates relative to the distribution of major faults and their time-varying slip potential could further unlock the subsurface potential to host larger volumes of CO₂. Such optimization is also relevant to the proper alignment of CO₂ storage projects with the spatial distribution of main industrial emitters in the study region (Bandilla and Celia, 2017). Regional pressure management through targeted brine extraction provides additional, technically viable means of enhancing storage capacity (Birkholzer et al., 2012). CO2BLOCKSEISM lays the foundation for addressing the performance of such mitigation measures and optimizing them to maintain fault stability with

the minimum number of pumping wells and amount of extracted brackish or saline water whose treatment and disposal may bear extra technical challenges and costs (Middleton et al., 2012). Thus, the developed analytical tool not only offers valuable insights into subsurface storage resources but also supports operational decision-making owing to its reasonable computational cost, accuracy and flexibility that enables considering a variety of scenarios under subsurface uncertainties. In addition to future developments to CO2BLOCKSEISM in the above-mentioned directions, we will apply this tool to major storage regions around the world to foster an improved understanding of the potential for CO₂ storage scale-up globally.

5. Conclusions

We have developed an analytical tool for screening subsurface CO₂ storage capacity subject to fault stability constraints. The tool draws on a probabilistic framework that enables rapid and reliable assessment of fault slip probabilities and possibly induced seismicity for different injection scenarios under subsurface uncertainties at regional scales. Testing the approach against seismicity induced by wastewater disposal in Oklahoma at comparable rates to Gt-scale CCS demonstrates the model capability to capture some important seismicity features. Yet, observations of numerous seismic events ruptured along previously unmapped faults point to limitations imposed on the application of this methodology by our insufficient knowledge of the subsurface prior to injection. The application of the tool to storage resource assessment in southern Utsira Sand, Norway, shows that the fault slip criterion exerts more strict constraints on storage capacity compared to the commonly adopted tensile fracturing limit of the caprock. We find that this formation can safely accommodate nearly 12.5 Gt through continuous injection for 50 years at a constant rate per site of 10 Mt/y under open flow boundary conditions. The estimated storage capacity corresponds to a

maximum pressure build-up of 1.7 MPa, which is much smaller than the overpressure that the caprock can withstand in the order of 5.6 MPa. Insights gained into the subsurface structural complexities through co-injection monitoring offer the opportunity to continuously update accessible CO₂ storage resources. Extension of the analysis to global storage resource assessment would develop a clear understanding of CCS scale-up that can be safely attained and will be the subject of our future studies.

Acknowledgements

I.R.K. and S.K. acknowledge funding from the Engineering and Physical Sciences Research Council through the UKRI Postdoc Guarantee Award THMC4CCS [Grant number EP/X026019/1]. S.D.S. acknowledges funding from MICIU/AEI /10.13039/501100011033 and from "European Union Next Generation EU/PRTR" through the 'Ramón y Cajal' fellowship (reference RYC2021-032780-I), and from "ERDF, EU" through the 'HydroPoreII' project (reference PID2022-137652NB-C44).

Data availability

The scripts of the tool CO2BLOCKSEISM, the input files used in this study and all the produced material are available at the repository <https://github.com/imanrahimzadeh/CO2BLOCKSEISM>.

References

Abercrombie, R.E., 2021. Resolution and uncertainties in estimates of earthquake stress drop and energy release. *Phil. Trans. R. Soc. A* 379(2196), 20200131.

<https://doi.org/10.1098/rsta.2020.0131>

Alt, R.C., Zoback, M.D., 2017. In situ stress and active faulting in Oklahoma. *Bull. Seismol. Soc. Am.* 107(1), 216-228. <https://doi.org/10.1785/0120160156>

Altunin, V., Sakhabetdinov, M., 1972. Viscosity of liquid and gaseous carbon dioxide at temperatures 220-1300 K and pressure up to 1200 bar. *Teploenergetika*, 8:85-89.

Bachu, S., 2015. Review of CO₂ storage efficiency in deep saline aquifers. *Int. J. Greenhouse Gas Control* 40, 188-202. <https://doi.org/10.1016/j.ijggc.2015.01.007>

Bandilla, K.W., Celia, M.A., 2017. Active pressure management through brine production for basin-wide deployment of geologic carbon sequestration. *Int. J. Greenh. Gas Control* 61, 155-167. <https://doi.org/10.1016/j.ijggc.2017.03.030>

Barton, C.A., Zoback, M.D., Moos, D., 1995. Fluid flow along potentially active faults in crystalline rock. *Geology*, 23(8), 683-686.

[https://doi.org/10.1130/0091-7613\(1995\)023<0683:FFAPAF>2.3.CO;2](https://doi.org/10.1130/0091-7613(1995)023<0683:FFAPAF>2.3.CO;2)

Birkholzer, J.T., Zhou, Q., Tsang, C.-F., 2009. Large-scale impact of CO₂ storage in deep saline aquifers: a sensitivity study on pressure response in stratified aquifer systems. *Int. J. Greenh. Gas Control* 3 (2), 181–194. <https://doi.org/10.1016/j.ijggc.2008.08.002>

Birkholzer, J.T., Cihan, A., Zhou, Q., 2012. Impact-driven pressure management via targeted brine extraction—conceptual studies of CO₂ storage in saline formations. *Int. J. Greenh. Gas Control* 7, 168-180. <https://doi.org/10.1016/j.ijggc.2012.01.001>

Bommer, J.J., 2022. Earthquake hazard and risk analysis for natural and induced seismicity: towards objective assessments in the face of uncertainty. *Bull. Earthquake Eng.* 20(6), 2825-3069. <https://doi.org/10.1007/s10518-022-01357-4>

Bommer, J.J., Verdon, J.P., 2024. The maximum magnitude of natural and induced earthquakes. *ESS Open Archive*. 10.22541/essoar.171826172.29972480/v1

Byerlee, J., 1978. Friction of rocks. *Pure Appl. Geophys.* 116, 615-626.
https://doi.org/10.1007/978-3-0348-7182-2_4

Chatelan, L., Thibeau, S., Frailey, S., 2023. Application of the storage resources management system to a regional open aquifer using a notional project. *Int. J. Greenhouse Gas Control* 129, 103959. <https://doi.org/10.1016/j.ijggc.2023.103959>

Darold, A.P., Holland, A.A., 2015. Preliminary Oklahoma fault orientations, Oklahoma Geol. Surv. Open-File Rept. OF4-2015.

Dentz, M., Tartakovsky, D.M., 2009. Abrupt-interface solution for carbon dioxide injection into porous media. *Transp. Porous Med.* 79 (1), 15–27. <https://doi.org/10.1007/s11242-008-9268-y>

De Simone, S., Jackson, S.J., Krevor, S., 2019. The error in using superposition to estimate pressure during multi-site subsurface CO₂ storage. *Geophys. Res. Lett.* 46 (12), 6525–6533.
<https://doi.org/10.1029/2019GL082738>

De Simone, S., Kivi, I. R., Min, K. B., Rutqvist, J., 2023. Induced seismicity in EGS: Observations and triggering mechanisms. In D. Chandrasekharam, & A. Baba (Eds.), *Enhanced Geothermal Systems (EGS)* (pp. 111-149). London: CRC Press.

De Simone, S., Krevor, S., 2021. A tool for first order estimates and optimisation of dynamic storage resource capacity in saline aquifers. *Int. J. Greenhouse Gas Control* 106, 103258.

<https://doi.org/10.1016/j.ijggc.2021.103258>

Elenius, M., Skurtveit, E., Yarushina, V., Baig, I., Sundal, A., Wangen, M., Landschulze, K., Kaufmann, R., Choi, J.C., Hellevang, H., Podladchikov, Y., 2018. Assessment of CO₂ storage capacity based on sparse data: Skade Formation. *Int. J. Greenhouse Gas Control* 79, 252-271.

<https://doi.org/10.1016/j.ijggc.2018.09.004>

Ehlig-Economides, C., Economides, M.J., 2010. Sequestering carbon dioxide in a closed underground volume. *J. Petr. Sci. Eng.* 70, 123–130. <https://doi.org/10.1016/j.petrol.2009.11.002>

Ellsworth, W.L., 2013. Injection-induced earthquakes. *Science* 341(6142), 1225942.

[10.1126/science.1225942](https://doi.org/10.1126/science.1225942)

Eshelby, J.D., 1957. The determination of the elastic field of an ellipsoidal inclusion, and related problems. *Proc. R. Soc. Lond. Ser. Math. Phys. Sci.* 241, 376–396.

<https://doi.org/10.1098/rspa.1957.0133>

Firoozmand, H., Leonenko, Y., 2022. An analytical approach to the technical and economical optimization of CO₂ sequestration in saline aquifers with simultaneous brine production. *J. Cleaner Prod.* 372, 133453. <https://doi.org/10.1016/j.jclepro.2022.133453>

Ganjdanesh, R., Hosseini, S.A., 2018. Development of an analytical simulation tool for storage capacity estimation of saline aquifers. *Int. J. Greenhouse Gas Control* 74, 142–154.

<https://doi.org/10.1016/j.ijggc.2018.04.017>

Gasda, S.E., Wangen, M., Bjørnara, T.I., Elenius, M.T., 2017. Investigation of caprock integrity due to pressure build-up during high-volume injection into the Utsira formation. *Energy Procedia*, 114, 3157-3166. <https://doi.org/10.1016/j.egypro.2017.03.1444>

Ge, S., Saar, M.O., 2022. Induced seismicity during geoenery development—A hydromechanical perspective. *J. Geophys. Res.: Solid Earth* 127(3), e2021JB023141.

<https://doi.org/10.1029/2021JB023141>

Goebel, T.H.W., Weingarten, M., Chen, X., Haffener, J., Brodsky, E.E., 2017. The 2016 Mw5.1 Fairview, Oklahoma earthquakes: Evidence for long-range poroelastic triggering at > 40 km from fluid disposal wells. *Earth Planet. Sci. Lett.* 472, 50-61.

<https://doi.org/10.1016/j.epsl.2017.05.011>

Halland, E., Mujezinović, J., Riis, F. (Eds.), 2014. CO₂ Storage Atlas: Norwegian Continental Shelf. Norwegian Petroleum Directorate.

Healy, J.H., Rubey, W.W., Griggs, D.T., Raleigh, C.B., 1968. The denver earthquakes. *Science* 161(3848), 1301-1310. 10.1126/science.161.3848.1301

Healy, D., Hicks, S.P., 2022. De-risking the energy transition by quantifying the uncertainties in fault stability. *Solid earth* 13(1), 15-39. <https://doi.org/10.5194/se-13-15-2022>

Heidbach, O., Rajabi, M., Cui, X., Fuchs, K., Müller, B., Reinecker, J., Reiter, K., Tingay, M., Wenzel, F., Xie, F., Ziegler, M.O., 2018. The World Stress Map database release 2016: Crustal

stress pattern across scales. *Tectonophysics*, 744, 484-498.

<https://doi.org/10.1016/j.tecto.2018.07.007>

Hennings, P.H., Snee, J.E.L., Osmond, J.L., DeShon, H.R., Dommissie, R., Horne, E., Lemons, C., Zoback, M.D., 2019. Injection-induced seismicity and fault-slip potential in the Fort Worth Basin, Texas. *Bull. Seismol. Soc. Am.* 109(5), 1615-1634. <https://doi.org/10.1785/0120190017>

Herzog, H.J., 2011. Scaling up carbon dioxide capture and storage: From megatons to gigatons. *Energy Econ.* 33(4), 597-604. <https://doi.org/10.1016/j.eneco.2010.11.004>

Hill, R.G., Weingarten, M., Langenbruch, C., Fialko, Y., 2024. Mitigation and optimization of induced seismicity using physics-based forecasting. arXiv preprint arXiv:2403.10675.

<https://doi.org/10.48550/arXiv.2403.10675>

Hovorka, S.D., Ambrose, W.A., Treviño, R.H., 2012. Sequestration of greenhouse gases in brine formations: CO₂ brine database. Gulf Coast Carbon Center (GCCC), Bureau of Economic Geology.

Huang, X., Bandilla, K.W., Celia, M.A., Bachu, S., 2014. Basin-scale modeling of CO₂ storage using models of varying complexity. *Int. J. Greenhouse Gas Control* 20, 73–86.

<https://doi.org/10.1016/j.ijggc.2013.11.004>

IPCC, 2022. Mitigation of Climate Change Climate Change 2022 Working Group III Contribution to the Sixth Assessment Report of the Intergovernmental Panel on Climate Change.

Kanamori, H., Anderson, D.L., 1975. Theoretical basis of some empirical relations in seismology. *Bull. Seismol. Soc. Am.* 65(5), 1073-1095.

<https://doi.org/10.1785/BSSA0650051073>

Kanamori, H., Brodsky, E.E., 2004. The physics of earthquakes. *Rep. Prog. Phys.* 67(8), 1429-1496. [10.1088/0034-4885/67/8/R03](https://doi.org/10.1088/0034-4885/67/8/R03)

Keranen, K.M., Weingarten, M., Abers, G.A., Bekins, B.A., Ge, S., 2014. Sharp increase in central Oklahoma seismicity since 2008 induced by massive wastewater injection. *Science*, 345(6195), 448-451. [10.1126/science.1255802](https://doi.org/10.1126/science.1255802)

Kirby, G.A., Chadwick, R.A., Holloway, S., 2001. Depth mapping and characterisation of the Utsira Sand Saline Aquifer, Northern North Sea. British Geological Survey Commissioned Report, CR/01/218. 26pp.

Kivi, I.R., Boyet, A., Wu, H., Walter, L., Hanson-Hedgecock, S., Parisio, F., Vilarrasa, V., 2023. Global physics-based database of injection-induced seismicity. *Earth Syst. Sci. Data* 15(7), 3163-3182. <https://doi.org/10.5194/essd-15-3163-2023>

Kivi, I.R., Makhnenko, R.Y., Oldenburg, C.M., Rutqvist, J. and Vilarrasa, V., 2022. Multi-layered systems for permanent geologic storage of CO₂ at the gigatonne scale. *Geophys. Res. Lett.* 49(24), e2022GL100443. <https://doi.org/10.1029/2022GL100443>

Kivi, I.R., Vilarrasa, V., Kim, K.I., Yoo, H., Min, K.B., 2024. On the role of poroelastic stressing and pore pressure diffusion in discrete fracture and fault system in triggering post-injection seismicity in enhanced geothermal systems. *Int. J. Rock Mech. Min. Sci.* 175, 105673. <https://doi.org/10.1016/j.ijrmms.2024.105673>

Kroll, K.A., Cochran, E.S., Murray, K.E., 2017. Poroelastic properties of the Arbuckle Group in Oklahoma derived from well fluid level response to the 3 September 2016 Mw 5.8 Pawnee and 7 November 2016 Mw 5.0 Cushing earthquakes. *Seismol. Res. Lett.* 88(4),963-970.

<https://doi.org/10.1785/0220160228>

Langenbruch, C., Zoback, M.D., 2016. How will induced seismicity in Oklahoma respond to decreased saltwater injection rates?. *Sci. Adv.* 2(11), e1601542. [10.1126/sciadv.1601542](https://doi.org/10.1126/sciadv.1601542)

Langenbruch, C., Weingarten, M., Zoback, M.D., 2018. Physics-based forecasting of man-made earthquake hazards in Oklahoma and Kansas. *Nat. Commun.* 9(1), 3946.

<https://doi.org/10.1038/s41467-018-06167-4>

Langenbruch, C., Moein, M.J., Shapiro, S.A., 2024. Are maximum magnitudes of induced earthquakes controlled by pressure diffusion?. *Phil. Trans. R. Soc. A* 382(2276), 20230184.

<https://doi.org/10.1098/rsta.2023.0184>

Lindeberg, E., Vuillaume, J.F., Ghaderi, A., 2009. Determination of the CO₂ storage capacity of the Utsira formation. *Energy Procedia*, 1(1), 2777–2784.

<https://doi.org/10.1016/j.egypro.2009.02.049>

Mathias, S.A., de Miguel, G.J.G.M., Thatcher, K.E., Zimmerman, R.W., 2011. Pressure buildup during CO₂ injection into a closed brine aquifer. *Transp. Porous Med.* 89 (3), 383–397.

<https://doi.org/10.1007/s11242-011-9776-z>

Middleton, R.S., Keating, G.N., Stauffer, P.H., Jordan, A.B., Viswanathan, H.S., Kang, Q.J., Carey, J.W., Mulkey, M.L., Sullivan, E.J., Chu, S.P., Esposito, R., 2012. The cross-scale science of CO₂ capture and storage: from pore scale to regional scale. *Energy Environ. Sci.* 5(6), 7328-

7345. <https://doi.org/10.1039/C2EE03227A>

Morgan, B.C., Murray, K.E., 2015. Characterizing small-scale permeability of the Arbuckle Group, Oklahoma. *Okla. Geol. Surv. Open-File Rept. OF2-2015*, 1-12.

Norbeck, J.H., Rubinstein, J.L., 2018. Hydromechanical earthquake nucleation model forecasts onset, peak, and falling rates of induced seismicity in Oklahoma and Kansas. *Geophys. Res. Lett.* 45(7), 2963-2975. <https://doi.org/10.1002/2017GL076562>

Nordbotten, J.M., Celia, M.A., Bachu, S., 2005. Injection and storage of CO₂ in deep saline aquifers: analytical solution for CO₂ plume evolution during injection. *Transp. Porous Med.* 58 (3), 339–360. <https://doi.org/10.1007/s11242-004-0670-9>

Norwegian Offshore Directorate, 2024. <https://www.sodir.no/>. (last accessed 27 August 2024)

Oklahoma Corporation Commission, 2017. Media advisory - regional earthquake response plan for central Oklahoma and expansion of the area of interest. [Available at <https://oklahoma.gov/occ/news/news-releases/news-archives/2016-news-releases.html>].

Park, J., Griffiths, L., Dautriat, J., Grande, L., Rodriguez, I.V., Iranpour, K., Bjørnarå, T.I., Moreno, H.M., Mondol, N.H., Sauvin, G., Sarout, J., 2022. Induced-seismicity geomechanics for controlled CO₂ storage in the North Sea (IGCCS). *Int. J. Greenhouse Gas Control*, 115, 103614. <https://doi.org/10.1016/j.ijggc.2022.103614>

Pettersson, P., Tveit, S., Gasda, S.E., 2022. Dynamic estimates of extreme-case CO₂ storage capacity for basin-scale heterogeneous systems under geological uncertainty. *Int. J. Greenhouse Gas Control*, 116, 103613. <https://doi.org/10.1016/j.ijggc.2022.103613>

Person, M., Banerjee, A., Rupp, J., Medina, C., Lichtner, P., Gable, C., Pawar, R., Celia, M., McIntosh, J., Bense, V., 2010. Assessment of basin-scale hydrologic impacts of CO₂ sequestration, Illinois basin. *Int. J. Greenhouse Gas Control*, 4(5), 840-854. <https://doi.org/10.1016/j.ijggc.2010.04.004>

Qin, J., Zhong, Q., Tang, Y., Rui, Z., Qiu, S., Chen, H., 2023. CO₂ storage potential assessment of offshore saline aquifers in China. *Fuel*, 341, 127681.

<https://doi.org/10.1016/j.fuel.2023.127681>

Raza, H., Kivi, I.R., França, G.S., Vilarrasa, V., 2023. Reservoir impoundment-triggered seismicity in Brazil: the case of M4. 0 Nova Ponte earthquake. *Sci. Rep.* 13(1), 22226.

<https://doi.org/10.1038/s41598-023-48924-6>

Ringrose, P.S., Furre, A.K., Gilfillan, S.M., Krevor, S., Landrø, M., Leslie, R., Meckel, T., Nazarian, B., Zahid, A., 2021. Storage of carbon dioxide in saline aquifers: physicochemical processes, key constraints, and scale-up potential. *Annu. Rev. Chem. Biomol. Eng.* 12(1), 471-

494. <https://doi.org/10.1146/annurev-chembioeng-093020-091447>

Ringrose, P.S., Meckel, T.A., 2019. Maturing global CO₂ storage resources on offshore continental margins to achieve 2DS emissions reductions. *Sci. Rep.*, 9(1), 1-10.

<https://doi.org/10.1038/s41598-019-54363-z>

Rodriguez Calzado, E., Hovorka, S.D., Bump, A.P., 2022. Mapping CO₂ injectivity potential within available CO₂ underground storage window in sedimentary rocks across the United States. In AGU Fall Meeting Abstracts, B25F-1610.

Rutqvist, J., 2012. The geomechanics of CO₂ storage in deep sedimentary formations. *Geotech. Geol. Eng.* 30, 525-551. <https://doi.org/10.1007/s10706-011-9491-0>

Schoenball, M., Ellsworth, W.L., 2017. Waveform-relocated earthquake catalog for Oklahoma and southern Kansas illuminates the regional fault network. *Seismol. Res. Lett.* 88(5), 1252-1258.

<https://doi.org/10.1785/0220170083>

Smith, A., Hampson, G., Krevor, S., 2024. Global analysis of geological CO₂ storage by pressure-limited injection sites. *Int. J. Greenhouse Gas Control*, 137, 104220.

<https://doi.org/10.1016/j.ijggc.2024.104220>

Snee, J.E.L., Zoback, M.D., 2018. State of stress in the Permian Basin, Texas and New Mexico: Implications for induced seismicity. *The Leading Edge* 37(2), 127-134.

<https://doi.org/10.1190/tle37020127.1>

Schultz, R., Beroza, G.C., Ellsworth, W.L., 2021. A risk-based approach for managing hydraulic fracturing-induced seismicity. *Science*, 372(6541), 504-507. 10.1126/science.abg5451

Spycher, N., Pruess, K., Ennis-king, J., (2003). CO₂-H₂O mixtures in the geological sequestration of CO₂. I. Assessment and calculation of mutual solubilities from 12 to 100 °C and up to 600 bar. *Geochim. Cosmochim. Acta* 67, 3015–3031. [https://doi.org/10.1016/S0016-](https://doi.org/10.1016/S0016-7037(03)00273-4)

[7037\(03\)00273-4](https://doi.org/10.1016/S0016-7037(03)00273-4)

Szulczewski, M.L., MacMinn, C.W., Herzog, H.J., Juanes, R., 2012. Lifetime of carbon capture and storage as a climate-change mitigation technology. *Proc. Natl. Acad. Sci. U.S.A.* 109 (14),

5185–5189. <https://doi.org/10.1073/pnas.1115347109>

USGS (2024). ANSS comprehensive earthquake catalog (ComCat).

<https://earthquake.usgs.gov/earthquakes/search/> (last accessed 27 August 2024)

van der Meer, L.G.H., Yavuz, F., 2009. CO₂ storage capacity calculations for the Dutch subsurface.

Energy Proc. 1, 2615–2622. <https://doi.org/10.1016/j.egypro.2009.02.028>

Verdon, J.P., Kendall, J.M., Stork, A.L., Chadwick, R.A., White, D.J., Bissell, R.C., 2013.

Comparison of geomechanical deformation induced by megatonne-scale CO₂ storage at Sleipner,

Weyburn, and In Salah. Proc. Natl. Acad. Sci. 110(30), E2762-E2771.
<https://doi.org/10.1073/pnas.1302156110>

Vilarrasa, V., Bolster, D., Dentz, M., Olivella, S., Carrera, J., 2010. Effects of CO₂ compressibility on CO₂ storage in deep saline aquifers. Transp. Porous Med. 85 (2), 619–639.
<https://doi.org/10.1007/s11242-010-9582-z>

Vilarrasa, V., Carrera, J., Olivella, S., Rutqvist, J., Laloui, L., 2019. Induced seismicity in geologic carbon storage. Solid Earth 10(3), 871-892. <https://doi.org/10.5194/se-10-871-2019>

Walsh III, F.R., Zoback, M.D., 2015. Oklahoma’s recent earthquakes and saltwater disposal. Sci. Adv. 1(5), e1500195. 10.1126/sciadv.1500195

Walsh III, F.R., Zoback, M.D., 2016. Probabilistic assessment of potential fault slip related to injection-induced earthquakes: Application to north-central Oklahoma, USA. Geology 44(12), 991-994. <https://doi.org/10.1130/G38275.1>

Weingarten, M., Ge, S., Godt, J.W., Bekins, B.A., Rubinstein, J.L., 2015. High-rate injection is associated with the increase in US mid-continent seismicity. Science 348(6241), 1336-1340. 10.1126/science.aab1345

Weingarten, J.S., Perkins, T.K., 1995. Prediction of sand production in gas wells: methods and Gulf of Mexico case studies. J. Pet. Technol. 47(07), 596-600. <https://doi.org/10.2118/24797-PA>

Xiang, Z., Moon, T., Oh, J., Si, G., Canbulat, I., 2024. Analytical investigations of in situ stress inversion from borehole breakout geometries. J. Rock Mech. Geotech. Eng. 16(7), 2375-2387.
<https://doi.org/10.1016/j.jrmge.2023.12.033>

- Yeck, W.L., Hayes, G.P., McNamara, D.E., Rubinstein, J.L., Barnhart, W.D., Earle, P.S., Benz, H.M., 2017. Oklahoma experiences largest earthquake during ongoing regional wastewater injection hazard mitigation efforts. *Geophys. Res. Lett.* 44(2), 711-717. <https://doi.org/10.1002/2016GL071685>
- Zahasky, C., Krevor, S., 2020. Global geologic carbon storage requirements of climate change mitigation scenarios. *Energy Environ. Sci.* 13(6), 1561-1567. <https://doi.org/10.1039/D0EE00674B>
- Zhai, G., Shirzaei, M., Manga, M., 2021. Widespread deep seismicity in the Delaware Basin, Texas, is mainly driven by shallow wastewater injection. *Proc. Natl. Acad. Sci.* 118(20), e2102338118. <https://doi.org/10.1073/pnas.2102338118>
- Zhang, Y., Jackson, C., Krevor, S., 2022. An Estimate of the Amount of Geological CO₂ Storage over the Period of 1996–2020. *Environ. Sci. Technol. Lett.* 9(8), 693-698. <https://doi.org/10.1021/acs.estlett.2c00296>
- Zhou, Q., Birkholzer, J.T., Tsang, C.F., Rutqvist, J., 2008. A method for quick assessment of CO₂ storage capacity in closed and semi-closed saline formations. *Int. J. Greenhouse Gas Control* 2(4), 626-639. <https://doi.org/10.1016/j.ijggc.2008.02.004>
- Zimmerman, R. (2018). *The Imperial College lectures in petroleum engineering. volume 5: Fluid flow in porous media.* World Scientific Publishing Europe. <https://doi.org/10.1142/q0146>
- Zweigle, P., Arts, R., Lothe, A.E., Lindeberg, E.B., 2004. Reservoir geology of the Utsira Formation at the first industrial-scale underground CO₂ storage site (Sleipner area, North Sea). *Geol. Soc. Spec. Publ.* 233(1), 165-180. <https://doi.org/10.1144/GSL.SP.2004.233.01.11>

Supporting Information for

A simplified physics model for estimating subsurface CO₂ storage resources constrained by fault slip potential

Iman R. Kivi¹, Silvia De Simone², Samuel Krevor¹

¹Department of Earth Science and Engineering, Imperial College London, London, UK

²Institute of Environmental Assessment and Water Research, Spanish National Research Council (IDAEA-CSIC), Barcelona, Spain

S1. Constraining horizontal stress magnitudes

Stress in the Earth's crust is constrained by the frictional strength of the faults meaning that the fault slip at this stress level prevents any further stress accumulation. Considering Coulomb failure theory, possible ranges of stress states at depth are given by

$$\frac{\sigma_1 - p}{\sigma_3 - p} \leq [(1 + \mu^2)^{1/2} + \mu]^2 \quad (\text{S1})$$

where μ is the friction coefficient of the fault, p is the pore pressure and σ_1 and σ_3 are the maximum and minimum principal stresses, respectively. Depending on stress regimes, i.e., normal, strike-slip or reverse, Eq. S1 can be rewritten as

$$\frac{\sigma_v - p}{\sigma_{hmin} - p} \leq [(1 + \mu^2)^{1/2} + \mu]^2, \quad \text{for normal stress regime} \quad (\text{S2})$$

$$\frac{\sigma_{Hmax} - p}{\sigma_{hmin} - p} \leq [(1 + \mu^2)^{1/2} + \mu]^2, \quad \text{for strike-slip stress regime} \quad (\text{S3})$$

$$\frac{\sigma_{Hmax} - p}{\sigma_v - p} \leq [(1 + \mu^2)^{1/2} + \mu]^2, \quad \text{for reverse stress regime} \quad (\text{S4})$$

where σ_v , σ_{hmin} and σ_{Hmax} are vertical and minimum and maximum horizontal stress components, respectively.

It is convenient to illustrate the allowable ranges of σ_{hmin} and σ_{Hmax} from Eqs. S2 to S4 using the so-called stress polygon (Zoback, 2010; Fig. S1). Equalities in these equations draw the lines bounding the polygon. Three stress regimes are divided by vertical and horizontal dashed lines, which cross each other at $\sigma_{hmin} = \sigma_{Hmax} = \sigma_v$. Stress buildup beyond the periphery of the stress polygon is not possible as it would result in fault slip, bringing the state of stress back into the polygon region.

We use the stress polygon concept to constrain horizontal stress magnitudes in Oklahoma. In the absence of direct σ_{hmin} measurements, this parameter can span the full possible range, from a minimum specified by frictional equilibrium in Eq. S2 (vertical line in the lower left of the polygon) to a maximum of σ_v . Considering an average σ_v gradient of 25 MPa/km, p gradient of 9.6 MPa/km and μ of 0.6, σ_{hmin} gradient ranges from 14.53 to 25 MPa/km. In order to maintain strike-slip stress conditions for all Monte Carlo realizations given the range of variation of σ_v , we simply narrow down the range of variation of σ_{hmin} gradient to a Gaussian distribution with an average of 20 MPa/km and a standard variation of 1 MPa/km. Note that the majority of values in a Gaussian distribution are contained within three standard deviations of the average.

We estimate σ_{Hmax} by assuming that the crust at the depths of investigation is critically stressed, meaning that the stress state is in frictional failure equilibrium and small pressure perturbations could rupture optimally oriented faults to slip as was observed to be the case in Oklahoma. Such stress criticality under a strike-slip regime is defined by the equality in Eq. S3 and corresponds to the diagonal line bounding the polygon on the upper left side (Fig. S1). Knowing the input

variables from the assigned statistical distributions, we separately calculate S_{Hmax} gradient for each Monte Carlo realization. The resulting distribution of σ_{Hmax} gradient is illustrated in Fig. S2.

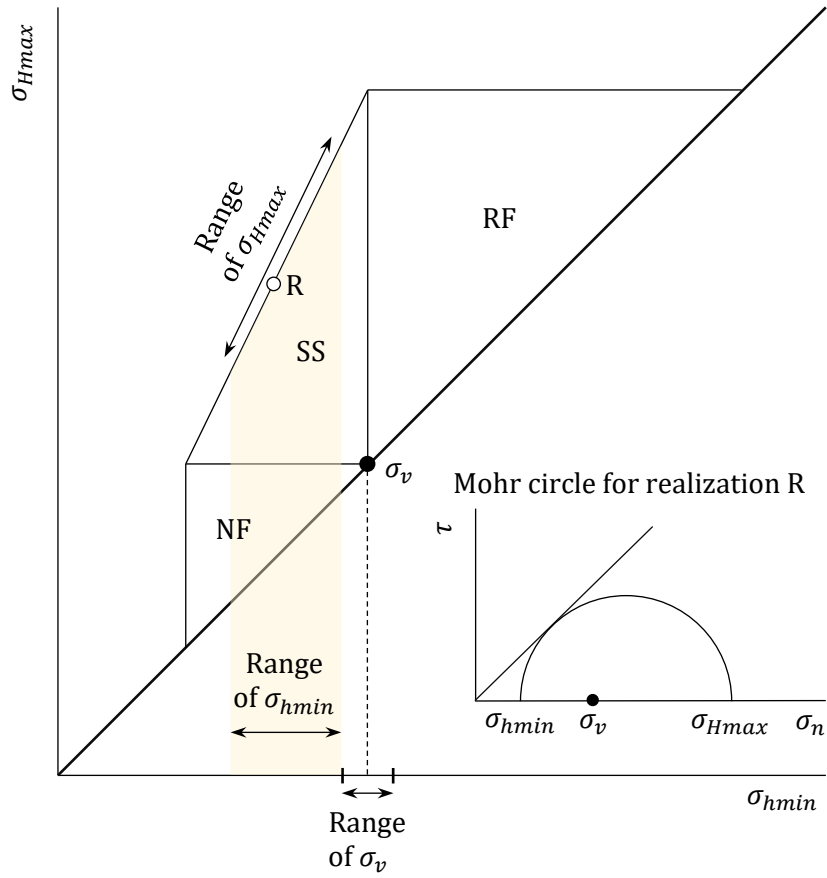


Fig. S1. Stress polygon defining allowable stress ranges in accordance with frictional strength of the Earth's crust. NF, SS and RF refer to normal, strike-slip and reverse faulting regimes, respectively.

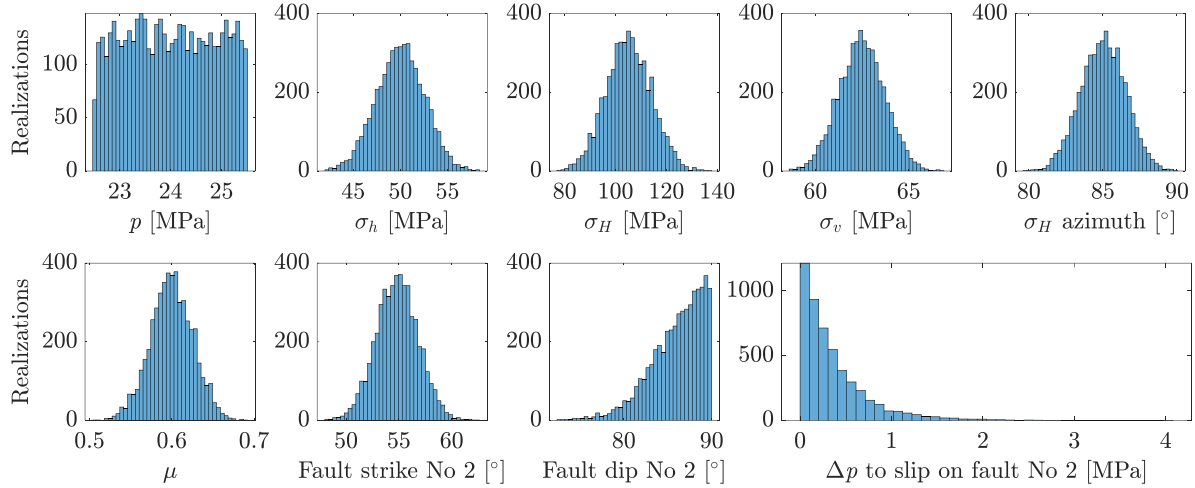


Fig. S2. Histograms illustrating statistical distributions of uncertain geomechanical variables used to develop Monte Carlo simulations for fault slip analysis in Oklahoma.

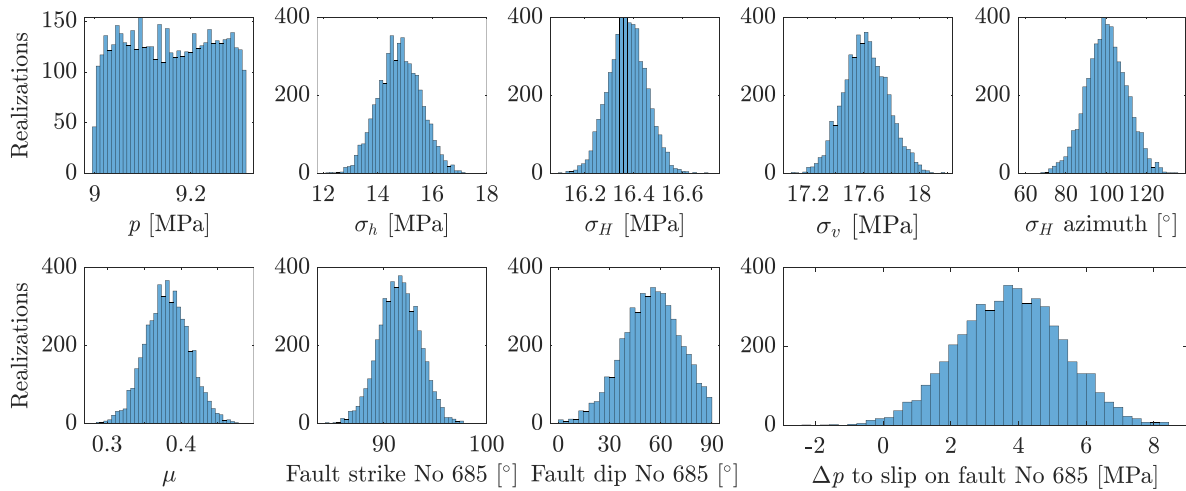


Fig. S3. Histograms illustrating statistical distributions of uncertain geomechanical variables used to develop Monte Carlo simulations for fault slip analysis in the Utsira storage unit.

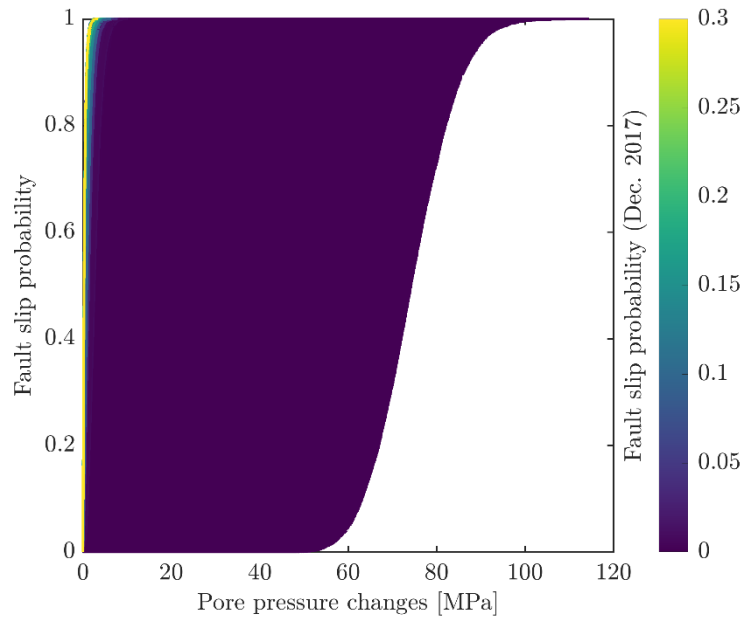


Fig. S4. Slip probability curves for each of the fault segments in the study area in Dec. 2017. The colorbar scale is adjusted to a maximum slip probability of 0.3 for better illustration purposes.

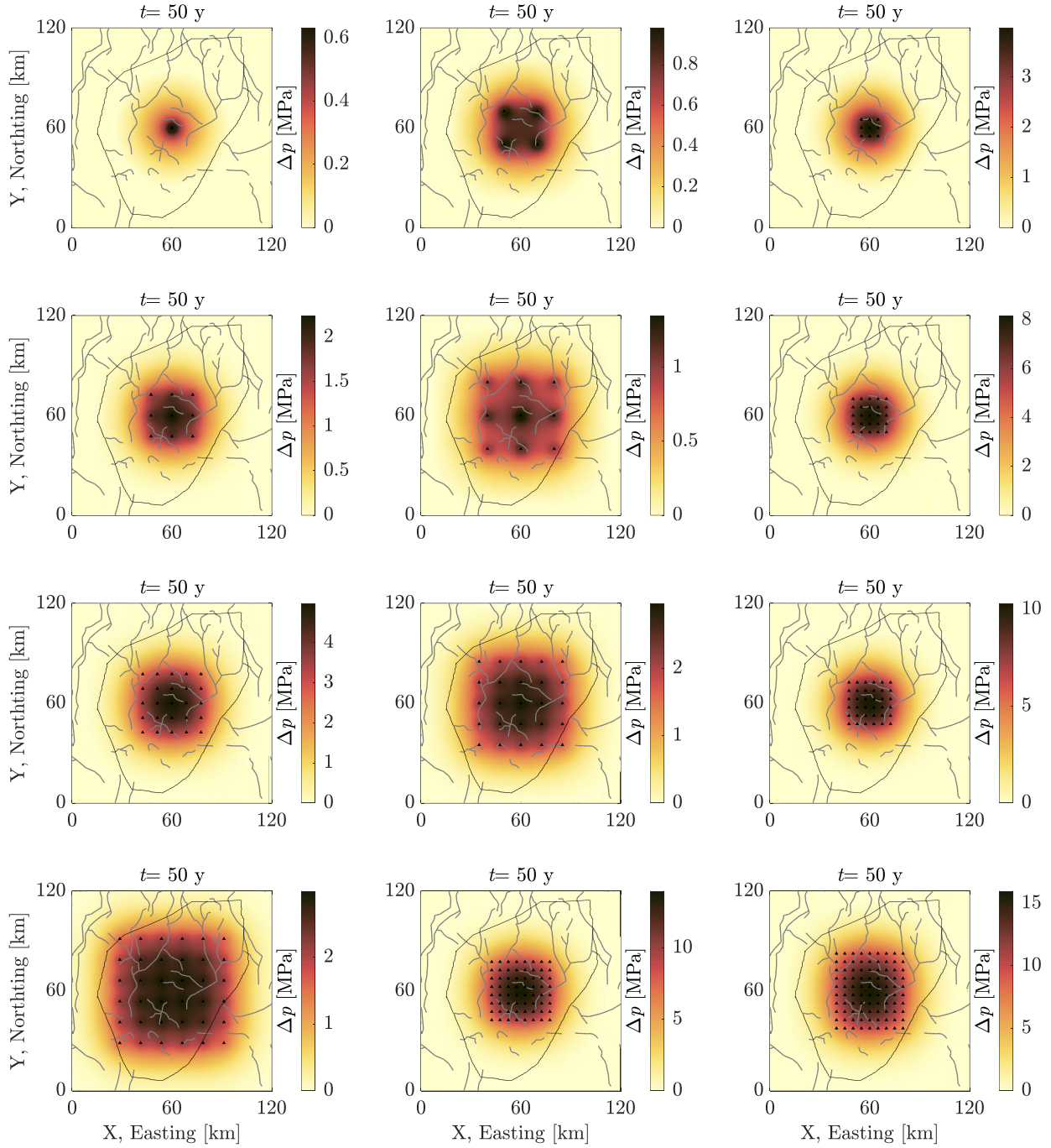


Fig. S5. Pore pressure changes calculated analytically for CO₂ injection into southern Utsira formation through different injection scenarios at a constant injection rate per well of 10 Mt/y.

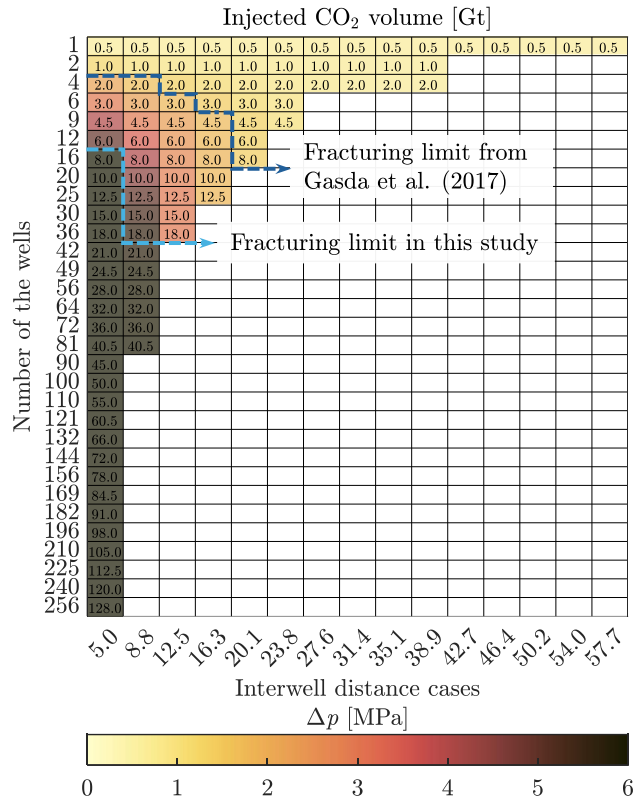


Fig. S6. Maximum injection-induced overpressure across the basin for different scenarios. Tensile fracturing limits of the caprock considered in this study and Gasda et al. (2017) are also illustrated with dashed blue lines. The color scale is adjusted to a maximum overpressure of 6 MPa for better illustration of storage capacity constrained by the caprock tensile fracturing limit.

References for SI

Zoback, M.D., 2010. Reservoir geomechanics. Cambridge university press.

Gasda, S.E., Wangen, M., Bjørnarå, T.I., Elenius, M.T., 2017. Investigation of caprock integrity due to pressure build-up during high-volume injection into the Utsira formation. Energy Procedia, 114, 3157-3166. <https://doi.org/10.1016/j.egypro.2017.03.1444>